

Evolution of the vibrational spectra of single-component solids with pressure: some universalities

Divya Srivastava and Subir K. Sarkar

School of Physical Sciences, Jawaharlal Nehru University, New Delhi - 110 067, INDIA

ABSTRACT

We have studied numerically the evolution of the zero temperature vibrational spectra of single-component solids with pressure using various model potentials with power law (type A) or exponential (type B) repulsive part. Based on these data and some semi-analytical calculations our principal results may be summarized as follows. For type A potentials: (i) The average frequency has a power law dependence on the pressure; (ii) The normalized vibrational density of states (NVDOS), with the average frequency as the unit of frequency, will saturate as the pressure keeps increasing. This asymptotic NVDOS is independent of the attractive component of the potential and hence define a universality class; and (iii) At higher pressures the Debye frequency and the average frequency have the same pressure dependence and this dependence is identical for the amorphous form and the two crystalline forms studied (FCC and HCP). For type B potentials, the above phenomenology will hold good to a good approximation over a wide range of intermediate pressures. We suggest a scaling form of the dispersion relations that would explain these observations. Various aspects of the evolution of sound speed with pressure are also studied. In particular we show that the Birch's law prescribing linear relationship between density and sound speed will hold good at very high pressures only in exceptional cases. We have also analyzed the data available in the literature from laboratory experiments and *ab initio* calculations and find that there is agreement with our conclusions which are derived from the study of model potentials. We offer explanation for this agreement.

PACS numbers: 05.70.Jk, 63.50.-x, 63.20.-e, 62.50.-p, 62.65.+k

I. Introduction

Study of the vibrational spectra of solids provides a rich variety of information. It helps us probe the interaction amongst the constituent particles of the solid. It also leads to an understanding of many properties measured at the macroscopic level such as sound propagation, specific heat etc.. In this sense vibrational spectra provide a bridge between the microscopic and the macroscopic aspects of solids. Unfortunately, understanding these spectra theoretically poses a very difficult challenge. As far as *computation* of the vibrational spectrum of any real material under a specified set of external conditions is concerned *ab initio* procedures based on electronic structure calculations are eminently possible nowadays for crystals if the unit cell size is not too big. But from the point of developing an understanding of the physics involved model-based studies offer some advantages. However, even if the interaction amongst the constituents is given, analytical calculation is made difficult first by the need to generate the geometry of the solid and secondly, in the case of amorphous systems, by having to compute the vibrational eigenvalue spectrum of a system with no spatial periodicity. It is not surprising therefore that a majority of even the model-based calculations are done on computers – especially when the amorphous state is involved[1-14]. Many details of the spectrum naturally depend on the potential of interaction applicable to the particular solid. Our interest in this paper is a study of the evolution of the vibrational spectra (and any other information derivable from it) of solids with externally applied pressure – with special emphasis on those aspects, qualitative or quantitative, that do not depend on some of the details of the potential. This study is done in the context of model single-component solids. The model potentials do not necessarily describe any particular material realistically. But we will argue that some predictions derived from studies based on these model potentials are applicable to real materials and we will make comparisons of these predictions with experimental data and *ab initio* calculations whenever permissible.

Pressure dependence of the crystalline vibrational spectrum has been studied in the literature both because of its fundamental physical interest and its relevance to problems of planetary geophysics [15-28]. Iron has been studied the most since it is the primary ingredient of the core of the earth. Interpretation of the data from experiments on geomagnetic or seismological properties of earth's interior depend crucially on the availability of reliable data on the relevant properties of iron at high pressure. Analysis of data on the evolution of the vibrational spectrum has to be done keeping in mind that there can be a change of crystal structure as pressure is increased. For example, iron changes from body-centered-cubic to hexagonal-close-packing at around 13 GPa.

For amorphous systems these studies have focussed largely on the boson peak [29-40] which stands for an excess of vibrational modes somewhere in the very low frequency part of the spectrum and the excess is in comparison to what would be expected from the Debye model. In particular we draw attention to [37] . In this laboratory experiment the vibrational spectrum of a disordered

polyisobutylene sample is measured at various pressures ranging from ambient to 1.4 GPa. The highest pressure applied causes a twenty percent increase of density and about a factor of two increase in the characteristic vibrational frequency. One result presented in this paper (see also [38-39]), analogues of which will be of central importance in our work, is that the plot of the reduced density of vibrational states against frequency can be made independent of applied pressure in the region of the boson peak with proper choice of units for the two axes. Also the variation of the Debye frequency with pressure was studied via measurements of longitudinal and transverse sound velocities (along with density). Our work is a computational version of experiments such as this – with the qualification that we study both crystalline and amorphous states and boson peaks are not studied at all due to the lack of adequate accuracy in the computation of the density of states at the lowest frequencies.

The other aspect that we investigate here is the speed of propagation of longitudinal and transverse acoustic waves. Study of sound velocities is of great interest in many physical situations and they may or may not include measurements of vibrational spectrum. In many cases the experimentally measured quantities are the elastic constants and this is then transcribed into statements on sound velocities. In yet another set of experiments inelastic scattering from phonons is used to determine sound speeds. A rather well established law regarding sound speed at high pressures is the Birch’s law which specifies linear relationship between density and sound velocity at high pressures. In the present work we address this aspect also and demonstrate that at extreme pressures this law holds only in exceptional situations.

Some of the key features of our work are as follows: (i) The applied pressure is always hydrostatic; (ii) We deal with a single-component system for which the interactions are given and have a relatively simple functional form; (iii) We study both amorphous and crystalline forms of matter for a given model potential. In the crystalline phase both FCC and HCP forms are supported by all the potentials used by us; (iv) The choice of potentials is a continuation of a previous set of studies where we demonstrated some universal properties of the statistical aspects of the vibrational spectra of amorphous clusters [41-42]; (v) Our calculations of vibrational modes are at zero temperature and hence we use the harmonic approximation. However, this should not be too much of a compromise since in the limit of very high pressure effect of a finite temperature is expected to be rather weak unless of course the temperature is very high, and finally, (vi) Considering the changes in density or characteristic vibrational frequency, our highest pressures are far higher than in any previous laboratory study or in any presently conceivable laboratory study.

The organization of this paper is as follows: In section II we present the methodologies of computation and analysis. Section III presents raw and scaled data on the evolution (with pressure) of vibrational spectra for representative potentials. We provide some representative data that make all the essential points. Also presented are data on the power law scaling of the average vibrational

frequency with pressure for various potentials. Section IV describes the results of a study of a nearest neighbor model of the crystalline vibrational spectrum in the case of FCC and HCP lattices. Section V contains a scaling ansatz and a discussion of its applicability in various situations. Section VI reports on the study of sound velocity with particular reference to the Birch's law - especially the domain and limits of its validity. Section VII contains some additional results relating to our study of amorphous systems. The main result that is reported relate to the existence of a pair of isosbestic points in the normalized vibrational spectrum when the exponent of the power law repulsive potential is varied (in the infinite pressure limit). Section VIII contains an analysis of data that is available in the literature and comparison with our predictions. Finally, section IX contains some concluding remarks.

II. Methodology

In order to prepare solid 'samples' in the model studies first we have to choose the interaction among the particles. All the potential energy expressions that we have used have the structure of an attractive part plus a repulsive part. The latter is always a sum over pairs i.e. is of the form $\sum_{All\ pairs} u(r_{ij})$ where u is the central pair potential; i and j label the particles in a pair for which r_{ij} denotes the pair separation. The attractive component is sometimes of the sum-over-pairs type. However, we also use non-sum- over-pairs potential in some cases for this part. The expression for u , the repulsive pair potential, will be of great importance in subsequent discussions. This function will always be of a power law form (i.e. $u(r)$ proportional to r^{-m}) or an exponentially decaying one (i.e. $u(r)$ proportional to $\exp(-r/r_0)$). We call them type A and type B potentials, respectively. The explicit forms of the potential energy expressions that we have used are: (i) Generalized Lennard-Jones potential: $\sum_{All\ pairs} (1/r_{ij}^{m_1} - 1/r_{ij}^{m_2})$. Here m_1 and m_2 are positive integers with m_1 greater than m_2 (m_1 is typically 12 or more). We will refer to this potential as GLJ(m_1, m_2). (ii) Morse potential: $\sum_{All\ pairs} (\exp(-2\alpha(r_{ij} - 1)) - \exp(-\alpha(r_{ij} - 1)))$. In this study the value of α will always be taken to be 9.0. (iii) Gupta potential: $A \sum_{All\ pairs} \exp[-p(r_{ij} - 1)] - \sum_{i=1}^N \sqrt{\sum_{j \neq i} \exp[-2q(r_{ij} - 1)]}$ with $A = 0.0376$, $p = 16.999$, and $q = 1.189$, and (iv) Sutton-Chen potential: $\sum_{All\ pairs} (1/r_{ij}^9) - \beta \sum_{i=1}^N \sqrt{\sum_{j \neq i} (1/r_{ij}^6)}$ with $\beta = 39.432$. The attractive parts of the expressions for the Gupta and Sutton-Chen potentials, as written here, are for a finite cluster with N particles. We, of course, use them in the context of the infinitely extended solid. The numerical values used for the parameters in the Sutton-Chen and Gupta potentials are those applicable to nickel. For all the potentials a suitable pair separation cutoff is employed. Also used is an appropriate interpolating function at this point. The latter ensures that derivatives upto second order are continuous at the cutoff distance. It can be seen that GLJ and Sutton-Chen potentials

are of type A whereas Morse and Gupta potentials are of type B. The choice of these particular potentials has been made basically as a continuation of their usage in some previous investigations into universal aspects of vibrational spectra [41-43]. Their analytical structures are more or less of the simplest types that incorporate the minimal requirements of physical plausibility and also lend themselves to efficient computation.

Face centered cubic (FCC) or hexagonal close packed (HCP) crystalline configurations at a particular pressure P_0 are produced by minimizing $(U + P_0\mathcal{V})$ with respect to the adjustable lattice parameters. Here U denotes the potential energy per unit cell of volume \mathcal{V} . For HCP structures the lattice parameters in and perpendicular to the plane of hexagonal symmetry are allowed to vary independently. But empirically it is found that at higher pressures the geometry of the HCP lattice is essentially indistinguishable from the ideal HCP lattice. This is a reflection of the isotropic non-bonding nature of the interactions that we are dealing with. In some parts of our analysis we will make use of this observation of ideality of the HCP lattice.

Following standard practice we approximate the amorphous state by a periodic system with as large a unit cell as possible. For us the unit cell contains 343 particles. By comparison with spectra with only 125 particles and spectra with as high as 6980 [44] particles in the unit cell we know that the spectra with 343 particles is very close to the infinite system limit except in the lowest eight percent or so of the spectral range (containing about two percent of all the modes) where the difference is somewhat noticeable. However, as we shall see, most of our results do not require a knowledge of this small part of the spectrum with high accuracy.

To prepare the amorphous solid 'samples' at various pressures we adopt the procedure outlined next. First choose the potential energy function. The unit cell containing 343 particles is defined by the edges \mathbf{a}_1 , \mathbf{a}_2 and \mathbf{a}_3 . We start with the stable FCC lattice at some relatively low pressure Q . This is then melted via a NPT -type configurational Monte-Carlo simulation with $P = Q$. In the simulation the variables are the three unit cell vectors and the 343 position vectors. From the liquid state we select a certain number of configurations spaced equally in time by a timescale substantially longer than the correlation time. Finally, using these configurations as initial guesses, conjugate gradient minimization is performed for the function $(U + Q\mathcal{V})$ with respect to the variables of the NPT simulation. Every state obtained via this minimization is characterized by the volume (Ω) and potential energy (ϵ) per particle. The states in the ϵ - Ω plane with the highest energies and the lowest densities correspond to the amorphous 'samples'(figure 1(a)). This is also crosschecked by examining the pair correlation function (figure (1b)).

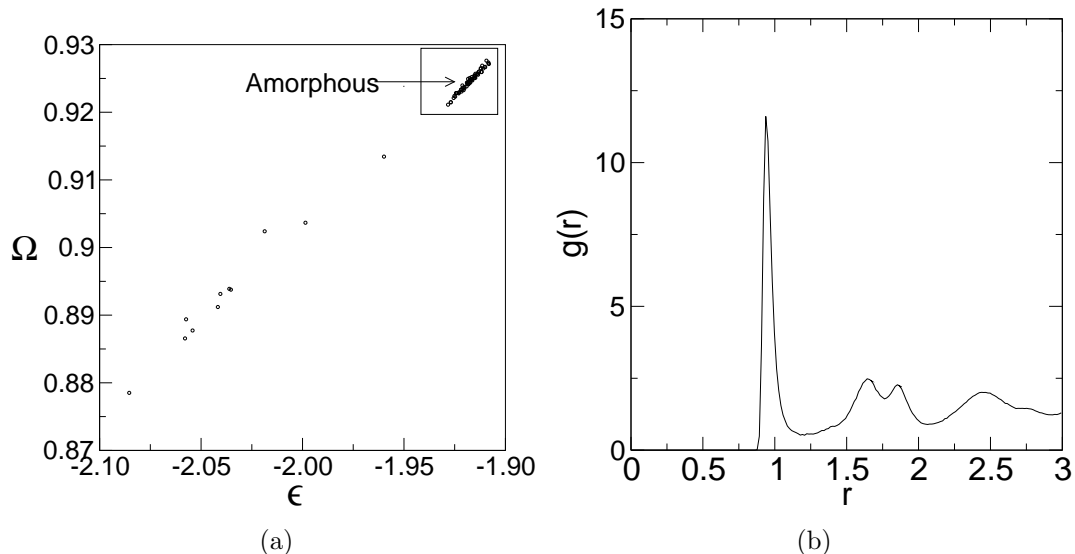


Figure 1: (a) Volume per particle(Ω) versus energy per particle(ϵ) for GLJ(12,6) at $P = 1$. The region inside the box corresponds to amorphous states. (b) Pair correlation function averaged over all the states in the amorphous region of (a)

Once the $T = 0$ amorphous solid geometries are obtained at the pressure Q , amorphous states at other pressures are generated by slow variation of pressure i.e. configurations for the minima at a particular pressure are used as the initial guesses for minimizations at a slightly different pressure. For each new pressure only the states with proper amorphous character are accepted – through an examination of the pair correlation function. We have checked that there is no statistically significant hysteresis in the generation of the amorphous states during pressurization and depressurization. Thus these states are reasonably uniquely defined as a function of pressure.

Once the stable solid geometries are generated computation of the vibrational density of states (VDOS) is done by diagonalizing the dynamical matrix and by integrating the resulting spectrum over the first Brillouin zone. Number of \mathbf{k} -points taken in the irreducible part of the first Brillouin zone for this integration varies from 108 in the amorphous case to not less than 11760 for the crystalline cases. For the amorphous case the DOS is averaged over all the local minima (between fifty and hundred in number).

To calculate the transverse (c_T) and longitudinal (c_L) speeds of sound propagation we use a method that avoids having to numerically evaluate the ratio of (frequency/length of wavevector) for a progressively shrinking sequence of wavevectors in a fixed direction – thus saving computational time and eliminating a significant source of numerical error. For the sake of completeness we briefly summarize the method [45] for a situation where there are N particles in the unit cell and they are not necessarily all of the same type – although in our applications the particles are identical in

all respects. Since we approximate the amorphous state by a periodic geometry with a sufficiently large unit cell the method described in the following is applicable to both crystalline and amorphous states.

For the unit cell associated with the Bravais lattice vector \mathbf{R} let the equilibrium position and the displacement from equilibrium position of the j^{th} atom ($j = 0, 1, 2, \dots, (N - 1)$) of mass m_j be $\mathbf{P}_j^{(\mathbf{R})}$ and $\mathbf{u}_j^{(\mathbf{R})}$, respectively.

If V is the overall potential energy of the system, define

$$\Phi_{\alpha\beta}(jj') = \frac{\partial^2 V}{\partial u_{\alpha}(\mathbf{R}_j) \partial u_{\beta}(\mathbf{R}_{j'})} \quad (1)$$

and

$$\mathbf{x}(jj') = \mathbf{P}_j^{(\mathbf{R}_2)} - \mathbf{P}_{j'}^{(\mathbf{R}_1)} \quad (2)$$

where $\mathbf{S} \equiv \mathbf{R}_2 - \mathbf{R}_1$ and the derivatives are evaluated at the equilibrium configuration. Now define

$$C_{\alpha\beta}^{(0)}(jj') = \frac{1}{\sqrt{m_j m_{j'}}} \sum_{\mathbf{R} \in \mathbf{BL}} \Phi_{\alpha\beta}(\mathbf{R}_{jj'}) \quad (3)$$

$$C_{\alpha\beta,\gamma}^{(1)}(jj') = \frac{-2\pi}{\sqrt{m_j m_{j'}}} \sum_{\mathbf{R} \in \mathbf{BL}} \Phi_{\alpha\beta}(\mathbf{R}_{jj'}) x_{\gamma}(\mathbf{R}_{jj'}) \quad (4)$$

and

$$C_{\alpha\beta,\gamma\lambda}^{(2)}(jj') = \frac{-4\pi^2}{\sqrt{m_j m_{j'}}} \sum_{\mathbf{R} \in \mathbf{BL}} \Phi_{\alpha\beta}(\mathbf{R}_{jj'}) x_{\gamma}(\mathbf{R}_{jj'}) x_{\lambda}(\mathbf{R}_{jj'}) \quad (5)$$

where \mathbf{BL} stands for the Bravais lattice.

Now consider the $(3N - 3) \times (3N - 3)$ matrix $C_{\alpha\beta}^{(0)}(jj')$ with j and $j' = 1, 2, \dots, (N - 1)$. Denote the inverse of this matrix by Π and then define the $3N \times 3N$ matrix Γ as follows

$$\begin{aligned} \Gamma_{\alpha\beta}(jj') &= \Pi_{\alpha\beta}(jj') & \text{if } j, j' \neq 0 \\ &= 0 & \text{otherwise} \end{aligned} \quad (6)$$

With these definitions the squares of the three sound velocities in the direction of the unit vector \hat{s} are given by the eigenvalues of a 3×3 matrix G where

$$G_{\alpha\beta} = \frac{1}{(\sum m_j)} \sum_{\gamma\lambda} s_{\gamma} s_{\lambda} ([\alpha\beta, \gamma\lambda] + \{\alpha\gamma, \beta\lambda\}) \quad (7)$$

with

$$[\alpha\beta, \gamma\lambda] = \frac{1}{8\pi^2} \sum_{jj'} (m_j m_{j'})^{\frac{1}{2}} C_{\alpha\beta,\gamma\lambda}^{(2)}(jj') \quad (8)$$

and

$$\{\alpha\gamma, \beta\lambda\} = -\frac{1}{4\pi^2} \sum_{jj'} \sum_{\mu\nu} \Gamma_{\mu\nu}(jj') \left(\sum_{j''} C_{\mu\alpha,\gamma}^{(1)}(jj'') \sqrt{m_{j''}} \right) \left(\sum_{j'''} C_{\nu\beta,\lambda}^{(1)}(j'j''') \sqrt{m_{j'''}} \right) \quad (9)$$

In general these speeds will not be isotropic – although for amorphous states the direction dependence, caused by the finite size of the unit cell, will be very weak. Hence, unless otherwise stated, average speed of sound (transverse or longitudinal) will always mean an average over ten thousand randomly (and isotropically) chosen directions. For amorphous states a further averaging is done over the configurations.

Finally, the Debye frequency ω_D is calculated through the formula $\omega_D^{-3} = B/(18n\pi^2)$ where B denotes the direction averaged value of $(1/c_1^3 + 1/c_2^3 + 1/c_3^3) - c_1, c_2$ and c_3 being the three speeds of sound in a particular direction. n denotes the number density of particles.

III. Results for the vibrational spectrum

A. Scaling law for the average frequency

Given the VDOS for a given potential and state of aggregation calculation of the average vibrational frequency is straightforward. Average frequency is defined as $\langle \omega \rangle = \int \omega G(\omega) d\omega / \int G(\omega) d\omega$ where $G(\omega)$ is the vibrational density of states. Please note that $G(\omega)$ is proportional to the size of the sample but $\langle \omega \rangle$ is not. This average is an indicator of the characteristic vibrational frequency of the system – although one can define other measures. Studies of variation of boson peak frequency or spectrum averaged frequency (or square of frequency, in case of studies in superconductivity) with pressure do exist. However, we are not aware of any investigations in the ultrahigh pressure regime that we are studying here. We find that in all the cases we have studied there is very strong support for a power law scaling of the average frequency with pressure, if we exclude the relatively low values of pressure. Thus $\langle \omega \rangle$ is proportional to P^δ where P is the applied hydrostatic pressure and δ is the scaling exponent. And this power law regime extends over a range where the applied pressure varies by a factor of the order of 100 or so and the frequency varies by a factor of about 10 (typically the range of our numerics is somewhat less for amorphous states since computation has to be done for a large number of local minima). Here we present the data only for one potential each of types A and B. Figures 2(a), 2(b) and 2(c) show the data for the GLJ(12,6) potential for the FCC, HCP and the amorphous state, respectively. In each case data for the full range of pressures is shown in the main display and that for the regime of high quality power law scaling is shown in the inset (in all cases the data points in the inset correspond to the high pressure end of the main display with no alteration in the number of data points). Figure 3 shows the corresponding data for the Morse potential. The quality of the power law fit should be evident from these figures.

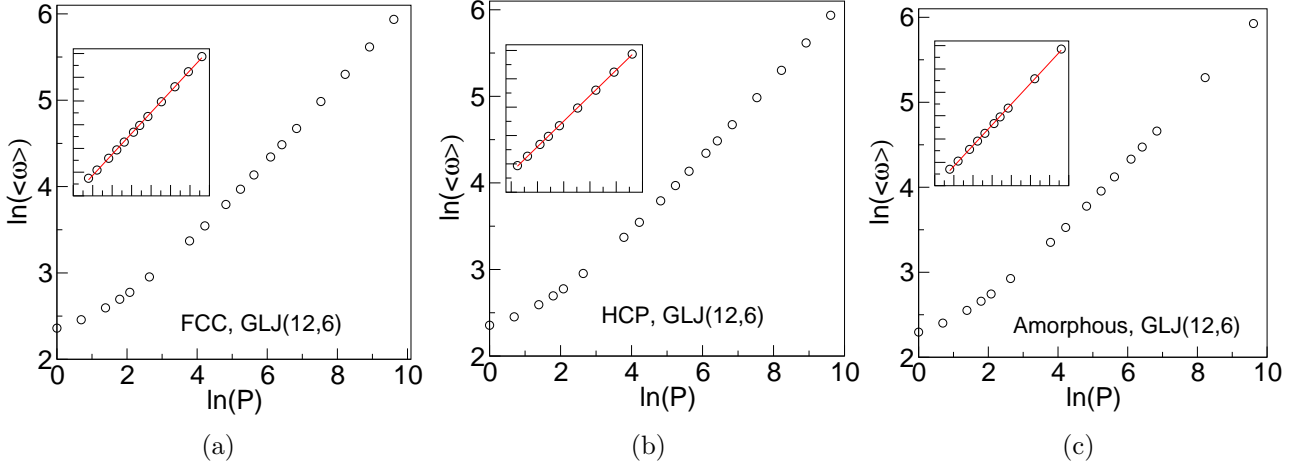


Figure 2: (a) Log of average frequency ($\langle \omega \rangle$) plotted as a function of log of pressure (P) for the FCC state of GLJ(12,6). The inset shows the precise linear dependence in the highest pressure region. (b) Same as in (a) but for the HCP state. (c) Same as in (a) but for the amorphous state.

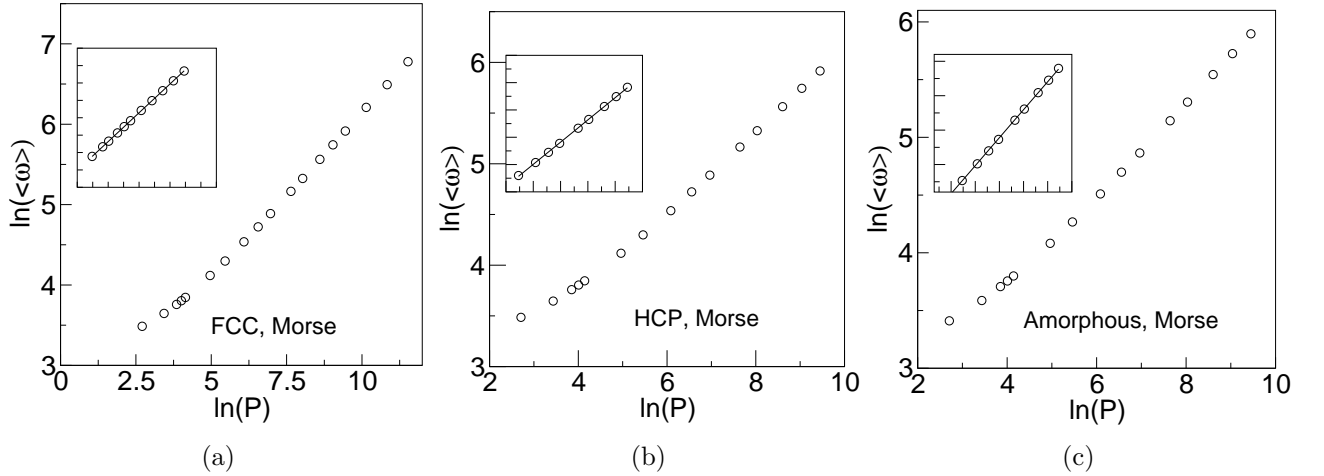


Figure 3: (a) Log of average frequency ($\langle \omega \rangle$) plotted as a function of log of pressure (P) for the FCC state of Morse potential. The inset shows the precise linear dependence in the highest pressure region. (b) Same as in (a) but for the HCP state. (c) Same as in (a) but for the amorphous state.

Table I provides the best fit values of the power law exponent (δ) for five different potentials. Two observations that can be made on the basis of the data in this table are: (1) The exponent seems to not depend on the state of aggregation, and (2) In all the cases the exponent is in a relatively narrow range below $1/2$.

Table I: Scaling exponent for the variation of average frequency with pressure

Potential	State of aggregation		
	AMORPHOUS	FCC	HCP
GLJ(12,6)	0.44	0.44	0.45
GLJ(12,10)	0.45	0.45	0.45
Sutton-Chen	0.44	0.45	0.44
Morse	0.41	0.41	0.41
Gupta	0.41	0.39	0.40

B. Shape convergence of the density of states function

Absolute vibrational density of states is proportional to the size of the sample and the scale of frequency depends on the particular potential at hand. Thus to compare VDOS at different pressures or perhaps for different potentials it is necessary to introduce a description that uses only dimensionless variables. This can be done in several ways but the one we use is to choose the unit of frequency to be $\langle \omega \rangle$, the average frequency. The dimensionless normalized frequency thus defined is denoted by $\nu (\equiv \omega / \langle \omega \rangle)$. The next step is to define a normalized density of states for normalized frequency (NDOSNF) $g(\nu) = \beta G(\nu \langle \omega \rangle)$ where β is chosen so that the integral $\int g(\nu) d\nu$ has a fixed value in all cases. It is clear that $g(\nu)$ describes the shape of the VDOS function. When the applied pressure goes up there is a steady increase in density as well as the characteristic frequency. In fact density increases by a factor which is often higher than four (and typically a little less for amorphous states) and the characteristic frequency goes up by a factor of around 15 (Density and characteristic frequency serve as physical measures of how large an applied pressure is). In fig.4(a) we show the VDOS function, denoted by $G(\omega)$, at five different pressures for the FCC state of the GLJ(12,6) potential. For each pressure the unit of VDOS is such that every curve has the same area under it (i.e. size of the 'sample' is fixed). Average frequency for the highest pressure is approximately twelve times the value for $P = 0$. This factor of increase in raw frequency is far higher than for any previous study (experimental or numerical) we are aware of. The raw VDOS plots of fig. 4(a) look quite disparate. However, if we now rescale the frequency variable in each curve by $\langle \omega \rangle$ for that curve and again plot the NDOSNF curves (area under each curve being unity) we get fig.4(b). It is seen that the VDOS function with *normalized* frequency as the argument changes rather little even with huge variations in the external pressure – even though the absolute scale of vibrational frequency does change by a large factor. In fact it seems that the

NDOSNF saturates asymptotically as pressure keeps increasing. This is suggested by fig.4(c) which reproduces the data in fig.4(b) but only for the three highest pressures. As a justification of the inference of saturation it may be noted that the absolute scale of frequency changes by a factor of two between the highest and the lowest pressure cases in fig.4(c). Figures 5 and 6 are the analogues of figure 4 for the HCP crystalline state and the amorphous state, respectively. It can be seen that the inference drawn from fig.4 for the FCC state is applicable also to the HCP and amorphous states i.e. there is saturation in the *shape* of the vibrational spectrum as pressure keeps growing.

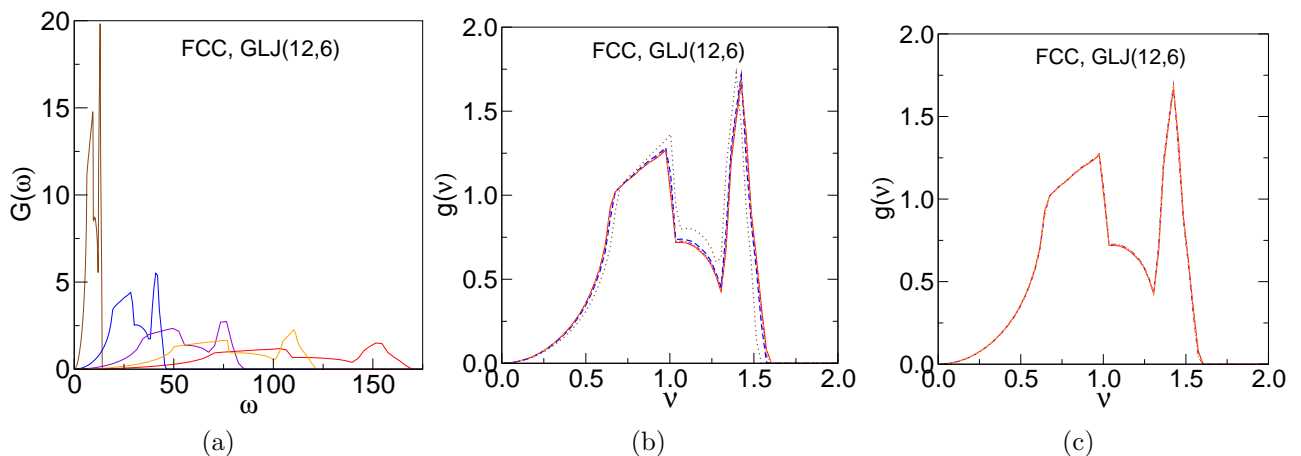


Figure 4: (a) Density of states (DOS) $G(\omega)$ for the FCC state of GLJ(12,6) is plotted against frequency (ω) for (from left to right) pressure $P = 0, 44, 188, 444$ and 932 . Area under every curve is the same. (b) For the FCC state normalized DOS $g(\nu)$ is plotted against normalized frequency (ν) for the same pressures as in (a). Area under every curve is unity. (c) The three highest pressure cases from (b) are reproduced to demonstrate apparent asymptotic convergence in the normalized DOS function as pressure keeps increasing.

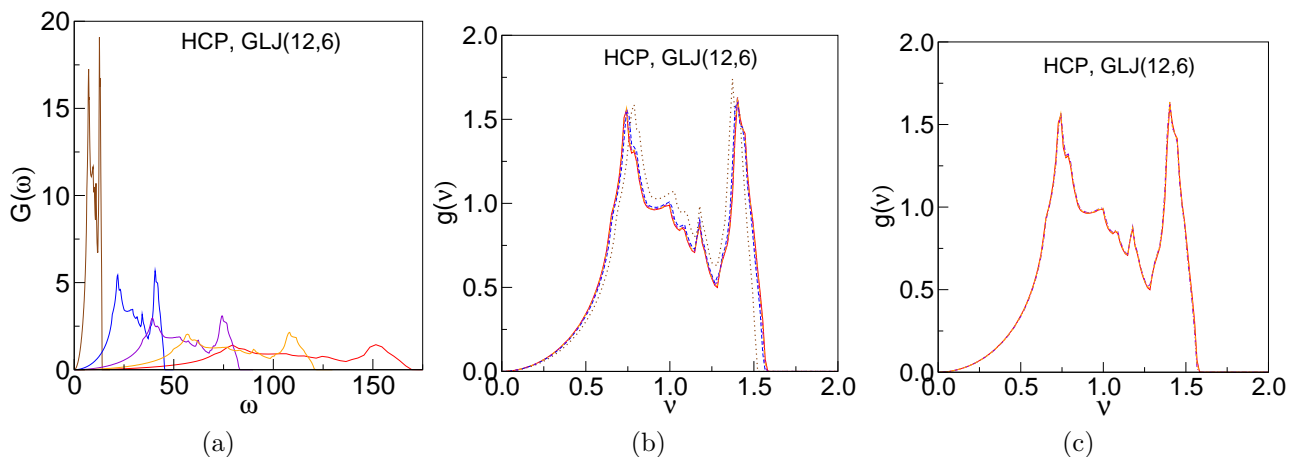


Figure 5: (a) Density of states (DOS) $G(\omega)$ for the HCP state of GLJ(12,6) is plotted against frequency (ω) for (from left to right) pressure $P = 0, 44, 188, 444$ and 932 . Area under every curve is the same. (b) For the HCP state normalized DOS $g(\nu)$ is plotted against normalized frequency (ν) for the same pressures as in (a). Area under every curve is unity. (c) The three highest pressure cases from (b) are reproduced to demonstrate apparent asymptotic convergence in the normalized DOS function as pressure keeps increasing.

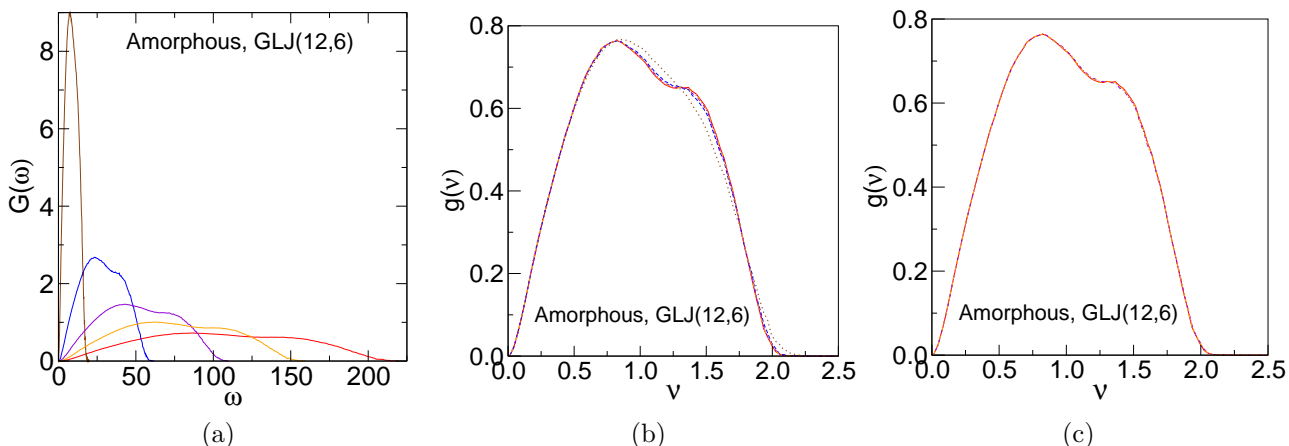


Figure 6: (a) Density of states (DOS) $G(\omega)$ for the amorphous state of GLJ(12,6) is plotted against frequency (ω) for (from left to right) pressure $P = 0, 44, 188, 444$ and 932 . Area under every curve is the same. (b) For the amorphous state normalized DOS $g(\nu)$ is plotted against normalized frequency (ν) for the same pressures as in (a). Area under every curve is unity. (c) The three highest pressure cases from (b) are reproduced to demonstrate apparent asymptotic convergence in the normalized DOS function as pressure keeps increasing.

Finally, figures 7, 8 and 9 show data analogous to figures 4,5 and 6 but for the Morse potential which belongs to type B. Inspection of figures 7(c), 8(c) and 9(c) make it immediately clear that the inference of asymptotic convergence of the NDOSNF is now less certain than in the case of

the GLJ(12,6) potential – even though the evidence may be considered to be quite strong by less rigorous standards.

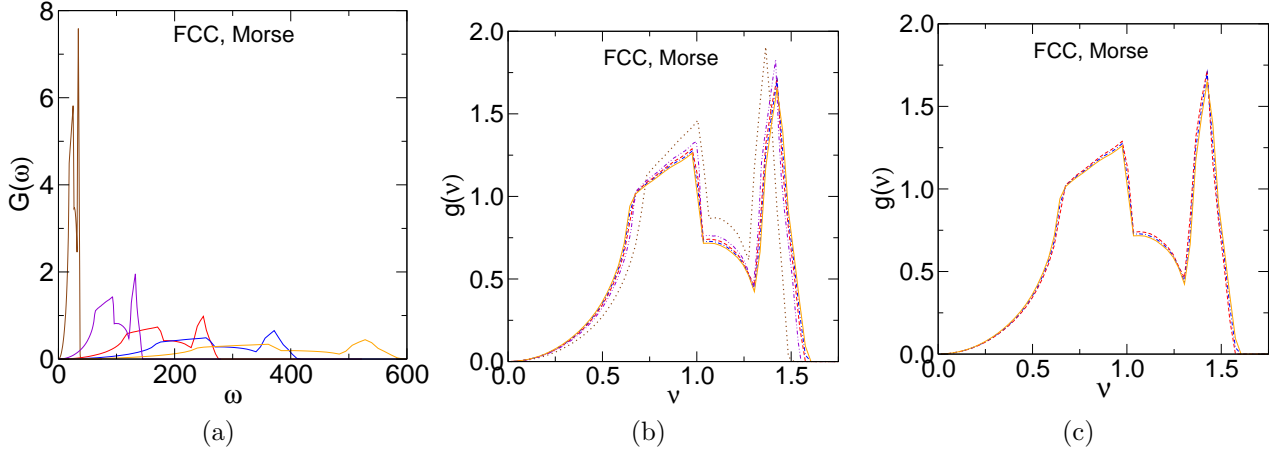


Figure 7: (a) Density of states (DOS) $G(\omega)$ for the FCC state of the Morse potential is plotted against frequency (ω) for (from left to right) pressure $P = 0, 439, 2087, 5453$ and 12689 . Area under every curve is the same. (b) For the FCC state normalized DOS $g(\nu)$ is plotted against normalized frequency (ν) for the same pressures as in (a). Area under every curve is unity. (c) The three highest pressure cases from (b) are reproduced to demonstrate the quality of evidence for asymptotic convergence in the normalized DOS function as pressure keeps increasing.

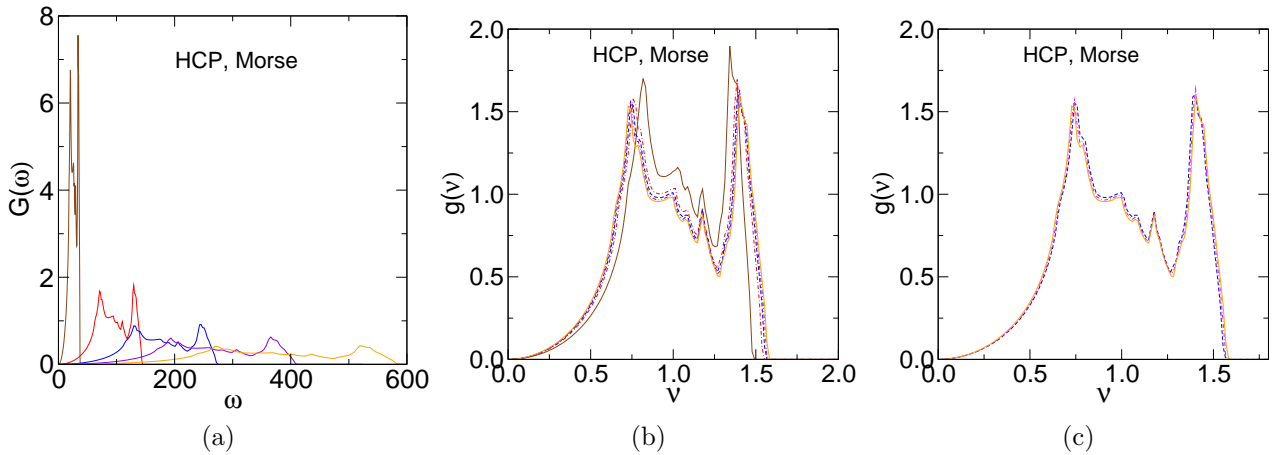


Figure 8: (a) Density of states (DOS) $G(\omega)$ for the HCP state of the Morse potential is plotted against frequency (ω) for (from left to right) pressure $P = 0, 439, 2087, 5453$ and 12689 . Area under every curve is the same. (b) For the HCP state normalized DOS $g(\nu)$ is plotted against normalized frequency (ν) for the same pressures as in (a). Area under every curve is unity. (c) The three highest pressure cases from (b) are reproduced to demonstrate the quality of evidence for asymptotic convergence in the normalized DOS function as pressure keeps increasing.

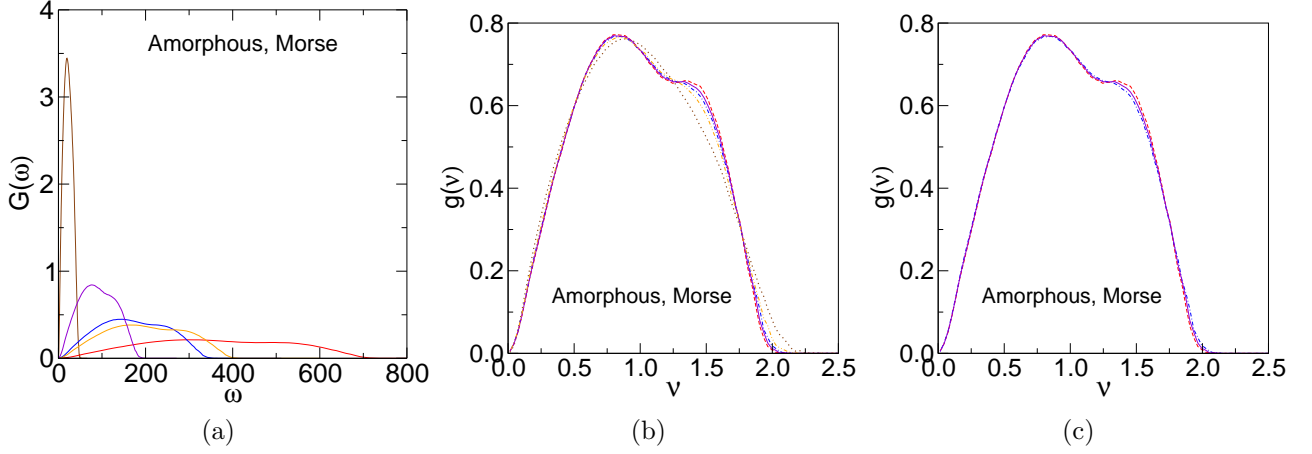


Figure 9: (a) Density of states (DOS) $G(\omega)$ for the amorphous state of the Morse potential is plotted against frequency (ω) for (from left to right) pressure $P = 0, 439, 2087, 5453$ and 12689 . Area under every curve is the same. (b) For the amorphous state normalized DOS $g(\nu)$ is plotted against normalized frequency (ν) for the same pressures as in (a). Area under every curve is unity. (c) The three highest pressure cases from (b) are reproduced to demonstrate the quality of evidence for asymptotic convergence in the normalized DOS function as pressure keeps increasing.

C. Average frequency and Debye frequency

Inspection of the low frequency limit of the data in the part (c) of figures 4 through 9 suggests that the proposal of asymptotic shape convergence made in section III(b) holds very accurately in that region. However, it needs to be remembered that the number of \mathbf{k} points used in the first Brillouin zone and, for the amorphous state, the size of the unit cell are not too large. These issues compromise the accuracy somewhat in the calculation of the low frequency limit of the density of states. However, using the method described in section II, we can calculate the sound velocities very accurately since we do not use the more commonly used method of numerically calculating the ratio ω/k in the limit of k going to zero. Hence an accurate alternative way of checking whether asymptotic shape convergence holds all the way down to the lowest frequencies is to calculate the Debye frequency and check whether, for higher pressures, it is proportional to the average frequency. If it is so it will indeed provide a supplementary confirmation of the primary implication of asymptotic shape invariance i.e. that there is only one scale of frequency. We have calculated the Debye frequency using the formula given in section II. Thus for each potential there are three average frequencies ($\langle \omega \rangle_{FCC}, \langle \omega \rangle_{HCP}$ and $\langle \omega \rangle_{Amor}$) and three Debye frequencies ($\omega^D_{FCC}, \omega^D_{HCP}$ and ω^D_{Amor}) corresponding to the three states of aggregation that we have studied. Based on our data we find that all these six frequencies are proportional to each other at higher pressures.

This can be seen from the figures 10 and 11 which present the data for the GLJ(12,6) and the Morse potential, respectively (for Sutton-Chen and Gupta potentials qualitatively indistinguishable results are obtained). Each of these two figures show five plots (only five independent ratios can be formed from six numbers) – with each plot showing the two elements of one pair plotted against each other. The best fit straight line passing through the origin helps us judge the validity of the statement of proportionality for each pair. Following the earlier observations regarding the power law scaling of the average frequency with respect to pressure we see that the same scaling is applicable for the Debye frequencies also.

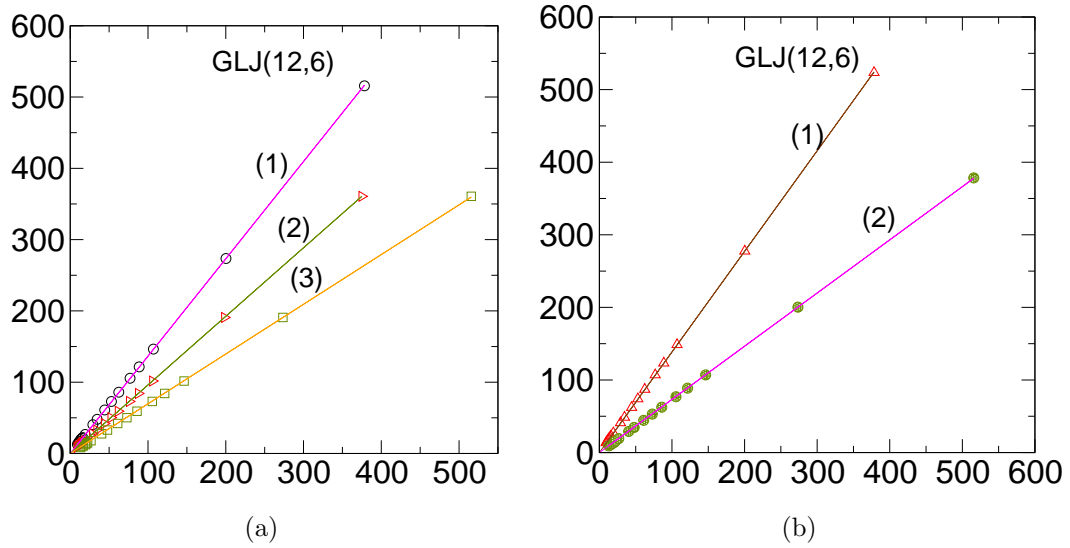


Figure 10: (a) Pairs of frequencies are plotted against each other at various pressures – as are the best fit straight lines passing through the origin. The potential is GLJ(12,6). (1): $\langle \omega \rangle_{FCC}$ (x-axis) vs. ω^D_{FCC} , (2): $\langle \omega \rangle_{Amor}$ vs. ω^D_{Amor} and (3) ω^D_{FCC} vs. ω^D_{Amor} . (b) Same as in (a) but the pairs plotted are: (1): $\langle \omega \rangle_{HCP}$ (x-axis) vs. ω^D_{HCP} and (2): ω^D_{FCC} vs. $\langle \omega \rangle_{HCP}$.

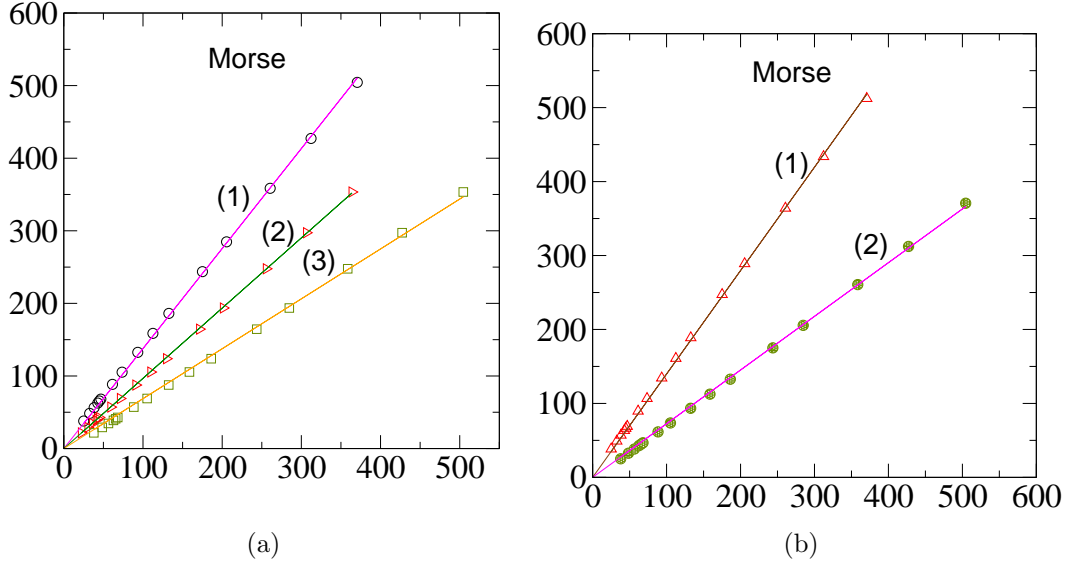


Figure 11: (a) For Morse potential pairs of frequencies are plotted against each other at various pressures – as are the best fit straight lines passing through the origin. (1): $\langle \omega \rangle_{FCC}$ (x-axis) vs. ω^D_{FCC} , (2): $\langle \omega \rangle_{Amor}$ vs. ω^D_{Amor} and (3) ω^D_{FCC} vs. ω^D_{Amor} . (b) Same as in (a) but the pairs plotted are: (1): $\langle \omega \rangle_{HCP}$ (x-axis) vs. ω^D_{HCP} and (2): ω^D_{FCC} vs. $\langle \omega \rangle_{HCP}$.

IV. Nearest neighbor model of vibrational spectrum for crystalline solids

In this section we demonstrate that a simple nearest neighbor model [see Chapter 22 of reference 46] for calculating the vibrational spectra of the FCC and the (ideal) HCP solids produces results in excellent agreement with the exact calculations at higher pressures. We show that the model is exact for a special limit of the family of type A potentials. For type B potentials it has a very wide range of validity but breaks down progressively more and more when pressure keeps increasing beyond a limit i.e. the domain of applicability is a wide range of *intermediate* pressures.

The first point to be noted is that the attractive part of the potential energy becomes smaller and smaller as a fraction of the repulsive part when the pressure keeps growing. This is a generic requirement that an expression of potential energy has to satisfy if it has to qualify as a descriptor of a stable solid. So, to describe a solid at higher pressures, we need to include only the repulsive part. In the present work this repulsive part is always a sum-over-pairs type expression. Let us denote this pair potential by $\phi(r)$.

Now, for a FCC solid or an ideal HCP solid, the geometry of arrangement of the particles does not depend on the applied pressure. We take the nearest neighbor distance to be the only independent parameter that changes with pressure. All other distances maintain a fixed ratio with respect to this distance. For example, for FCC solid the next nearest neighbor distance is always

$\sqrt{2}$ times the nearest neighbor distance. As stated earlier the repulsive part is always taken to be a sum-over-pairs type expression. But this sum is over *all* pairs to begin with. So it is obvious that in a situation in which the nearest neighbor contribution is far higher than the sum of all the non-nearest neighbor contributions a quantitatively adequate description of the vibrational spectrum can be given by including only the nearest neighbor interactions. For type A potentials, where $\phi(r)$ is proportional to r^{-m} , this is clearly true when the value of m is reasonably large (the lowest value we use is 9, for the Sutton-Chen potential). And the approximation becomes exact in the limit of m going to infinity. For type B potentials the full range of higher pressures can be subdivided into two ranges: intermediate and very high – the exact ranges under these two domains being controlled by the range of the exponential potential. To see why the nearest neighbor description works in the intermediate range of pressures (or the nearest neighbor distance) consider the ratio T_{nn}/T_{nnn} where T_{nn} and T_{nnn} represent the contributions of a nearest neighbor pair (separated by distance d) and a next nearest neighbor pair, respectively, to the total energy. With $\phi(r)$ being of the form $\exp(-\alpha r)$ for the type B potentials this ratio (θ) is $\exp((p-1)\alpha d)$ where p , the ratio of the next-nearest-neighbor distance over the nearest neighbor distance, is greater than unity by definition. For example, for FCC crystals, p is $\sqrt{2}$. Clearly, higher the value of θ , better is the nearest neighbor approximation. However, with increasing pressure, the nearest neighbor distance d goes down and so does θ – as can be seen from the expression of θ above. Exactly how big is the range of pressures for which θ is large enough is controlled by the value of α .

Let us now assume that we are in a situation where it is permissible to ignore the interactions beyond the nearest neighbor. In such a situation the vibrational spectrum can be calculated as follows:

A. FCC crystal

The frequencies of the three normal modes with wave vector \mathbf{k} are proportional to the square roots of the three eigenvalues of the 3×3 dynamical matrix

$$D(\mathbf{k}) = \sum_{\mathbf{R}} \sin^2 \left(\frac{1}{2} \mathbf{k} \cdot \mathbf{R} \right) [A\mathbf{I} + B\hat{\mathbf{R}}\hat{\mathbf{R}}] \quad (10)$$

where the sum is to be taken over the twelve nearest neighbors around $\mathbf{R} = \mathbf{0}$. $\hat{\mathbf{R}}$ is the unit vector in the direction of \mathbf{R} . \mathbf{I} is the 3×3 unit matrix and $\hat{\mathbf{R}}\hat{\mathbf{R}}$ is the diadic 3×3 matrix defined as $(\hat{\mathbf{R}}\hat{\mathbf{R}})_{\mu\nu} = \hat{\mathbf{R}}_{\mu}\hat{\mathbf{R}}_{\nu}$. A and B are defined to be equal to $2\frac{\phi'(d)}{d}$ and $2[\phi''(d) - \phi'(d)/d]$, respectively.

B. Ideal HCP crystal

Here there are two particles (located at \mathbf{p}_1 and \mathbf{p}_2) per unit cell and the algebra for calculating the dynamical matrix is somewhat more complicated than in the case of the FCC crystal. But the result can be summarized as follows:

The dynamical matrix $D(\mathbf{k})$ has the following structure:

$$D(\mathbf{k}) = \left[\begin{array}{c|c} (1,1) & (1,2) \\ \hline (2,1) & (2,2) \end{array} \right]$$

where (1,1),(1,2),(2,1) and (2,2) are all 3×3 matrices. (1,1) and (2,2) are identical matrices of which the element at the μ^{th} row and ν^{th} column is given by

$$\begin{aligned} & -\frac{\phi'(d)}{d} \left[\sum_{\mathbf{R} \in B} \left\{ \left(1 - d \frac{\phi''(d)}{\phi'(d)} \right) \hat{n}_\mu(\mathbf{R} + \mathbf{p}_2 - \mathbf{p}_1) \hat{n}_\nu(\mathbf{R} + \mathbf{p}_2 - \mathbf{p}_1) - \delta_{\mu\nu} \right\} \right. \\ & \left. + 2 \sum_{\mathbf{R} \in C} \left\{ \left(1 - d \frac{\phi''(d)}{\phi'(d)} \right) \hat{n}_\nu(\mathbf{R}) \hat{n}_\mu(\mathbf{R}) - \delta_{\mu\nu} \right\} \sin^2 \left(\frac{1}{2} \mathbf{R} \cdot \mathbf{k} \right) \right] \end{aligned}$$

where $\hat{n}_\alpha(\mathbf{t})$ is the α^{th} component of the unit vector in direction of vector \mathbf{t} . B and C are sets of vectors of the form $n_1 \mathbf{a}_1 + n_2 \mathbf{a}_2 + n_3 \mathbf{a}_3$ ($\mathbf{a}_1, \mathbf{a}_2$ and \mathbf{a}_3 are the edges of the unit cell). For the set B , $(n_1, n_2, n_3) = (-1, 0, -1), (-1, 0, 0), (0, -1, -1), (0, -1, 0), (0, 0, -1)$ and $(0, 0, 0)$ while for the set C , $(n_1, n_2, n_3) = (-1, 0, 0), (-1, 1, 0), (0, -1, 0), (0, 1, 0), (1, -1, 0)$ and $(1, 0, 0)$. In block (1,2) the element at the μ^{th} row and ν^{th} column is given by

$$-\frac{\phi'(d)}{d} \sum_{\mathbf{R} \in A} \left[\delta_{\mu\nu} - \left(1 - d \frac{\phi''(d)}{\phi'(d)} \right) \hat{n}_\mu(\mathbf{R} + \mathbf{p}_1 - \mathbf{p}_2) \hat{n}_\nu(\mathbf{R} + \mathbf{p}_1 - \mathbf{p}_2) \right] e^{-i\mathbf{k} \cdot \mathbf{R}}$$

where A contains the vectors $n_1 \mathbf{a}_1 + n_2 \mathbf{a}_2 + n_3 \mathbf{a}_3$ with $(n_1, n_2, n_3) = (0, 0, 0), (0, 0, 1), (0, 1, 0), (0, 1, 1), (1, 0, 0)$ and $(1, 0, 1)$. In block (2,1), the element at the μ^{th} row and ν^{th} column is given by

$$-\frac{\phi'(d)}{d} \sum_{\mathbf{R} \in B} \left[\delta_{\mu\nu} - \left(1 - d \frac{\phi''(d)}{\phi'(d)} \right) \hat{n}_\mu(\mathbf{R} + \mathbf{p}_2 - \mathbf{p}_1) \hat{n}_\nu(\mathbf{R} + \mathbf{p}_2 - \mathbf{p}_1) \right] e^{-i\mathbf{k} \cdot \mathbf{R}}$$

While constructing the NDOSNF the overall scale of the vibrational frequencies becomes irrelevant and hence it is clear that the only parameter controlling the NDOSNF for both FCC and ideal HCP crystals is the dimensionless number $\beta(d) \equiv 1 - d\phi''(d)/\phi'(d)$. Thus, if the nearest neighbor approximation is a valid one, two different potentials will have identical FCC (or ideal HCP) NDOSNF if the pressures are adjusted such that the value of the β parameter is identical for the two situations. This is illustrated in figure 12 where the FCC type NDOSNF are superposed for GLJ(12,6) at $P = 1864$ and for Morse potential at $P = 12689$, the (almost) common value of β being equal to 14.635.

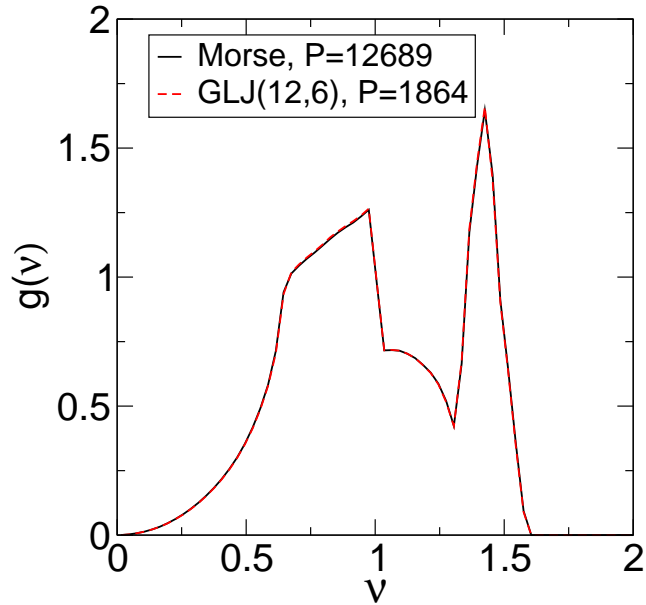


Figure 12: Normalized density of states $g(\nu)$ for normalized frequency (ν) are superposed for the GLJ(12,6) potential at $P = 1864$ and the Morse potential at $P = 12689$. The two spectra are essentially indistinguishable.

As we mentioned earlier the nearest neighbor approximation breaks down at the highest pressures if the potential is of type B. This is demonstrated in figure 13 for the Gupta potential. Fig.13(a) corresponds to a pressure where the nearest neighbor approximation is still a very good one. But for fig.13(b) the pressure is so high (the nearest neighbor distance being correspondingly short) that the breakdown of the nearest neighbor approximation is quite visible. Needless to say the agreement worsens progressively as the pressure increases even further.

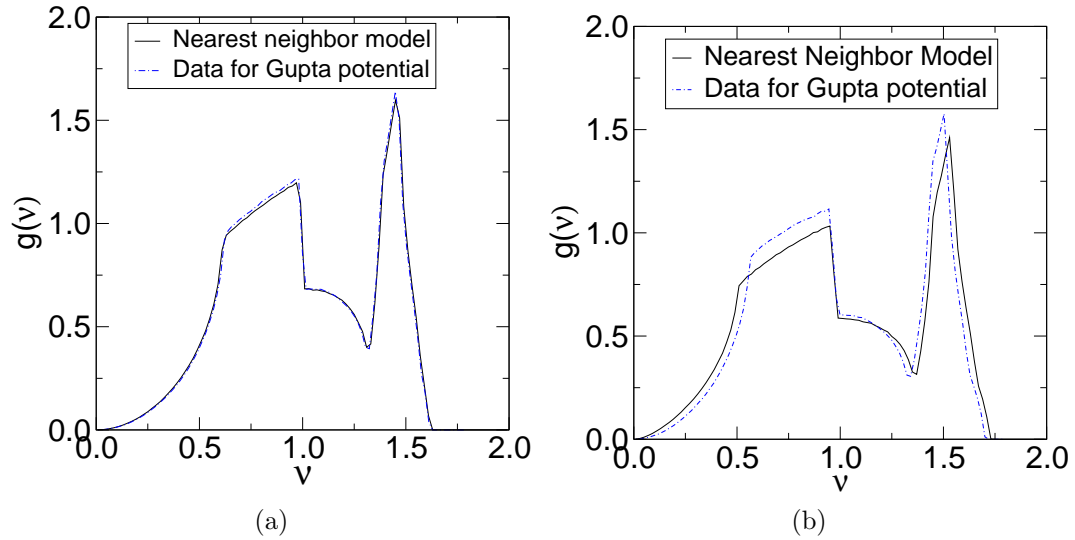


Figure 13: (a) Normalized density of states $g(\nu)$ for normalized frequency (ν) is shown for Gupta potential at $P = 1650$ and the prediction for this case from the nearest neighbor model. The agreement is very good. (b) Same as in (a) but for $P = 160000$. Now the disagreement with the prediction from the nearest neighbor model is quite prominent.

We have just described the procedure for calculating the NDOSNF for FCC and (ideal) HCP crystal in the nearest neighbor approximation for a given value of β . Two interesting aspects of this procedure are that: (i) In both the cases vibrational spectrum exists only for β greater than 8 i.e. for a value of β below this the dynamical matrix is not positive definite for all \mathbf{k} in the first Brillouin zone. There seems to be no singularity as β approaches the value of 8 from above. (ii) In the limit of β going to infinity the NDOSNF is well defined. The first observation is based on numerics and we do not have an analytical understanding of this behaviour at $\beta = 8$. We will see later that the second observation is what enables us to establish connection with experiments on real materials. Figures 14(a) and 14(b) show the evolution of the shape of the vibrational spectrum with change in the value of β within the framework of the nearest neighbor model for the FCC and the ideal HCP geometries, respectively. In both the cases the shape function shrinks without any change in the position of the center as β goes to infinity. Due to normalization there is a corresponding increase in the height of the function. One way to quantify this is to define a 'fatness coefficient' as the ratio of the standard deviation of the frequency to the mean frequency. We find that for both the FCC and the HCP geometries this coefficient changes from around 0.4 to 0.28 as β goes from its lowest permissible value to infinity. As would be expected from the existence of a well defined limit when β goes to infinity the dependence of the NDOSNF on β becomes very weak for the higher values of β .

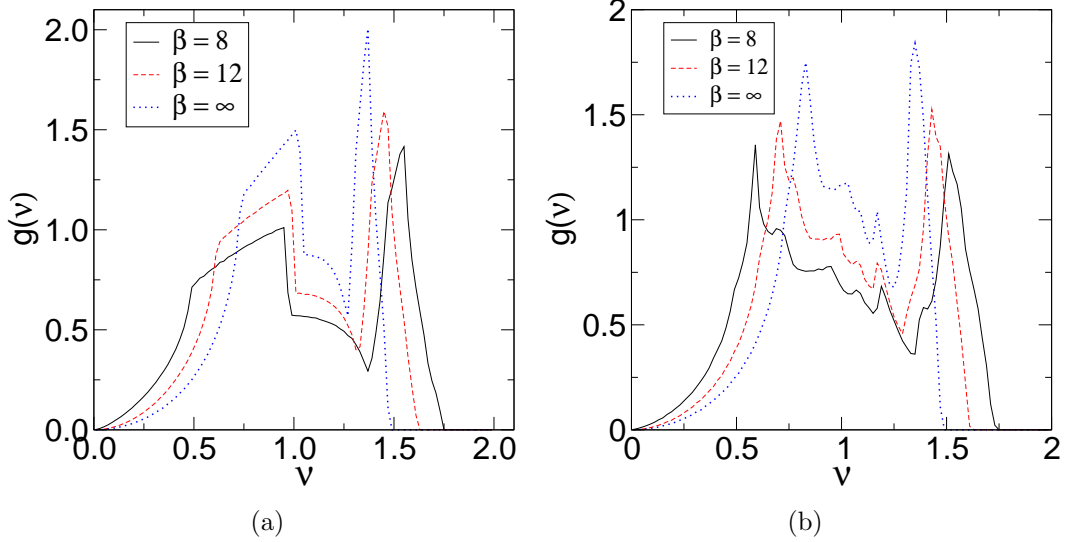


Figure 14: Evolution of the NDOSNF function for the nearest neighbor model with the control parameter β . For the sake of clarity plots are shown for only three values of β . (a) FCC (b) HCP.

V. Scaling ansatz for the dispersion relation

The observation of shape convergence for the entire vibrational spectrum and the proportionality of the average and Debye frequencies for the various states of aggregation, made in sections III.B and III.C, can be explained on the basis of a scaling ansatz regarding the dispersion relations. The ansatz is that, at higher pressures,

$$\omega_i(\mathbf{k}) = W(P)F_i(\mathbf{k}n^{-1/3}) \quad (11)$$

where n is the number density of particles and $W(P)$ depends on the potential energy function but not on the state of aggregation. i is the index labeling a particular branch of the dispersion relations. For every value of i the function F_i , which depends on the state of aggregation, is a positive definite function whose domain of definition is finite and is independent of pressure. Here we assume that the shape of the first Brillouin zone does not change once the applied pressure becomes sufficiently high. In that case its linear dimension becomes proportional to $n^{1/3}$. Also, for every i , F_i is bounded above. Hence, for the sake of definiteness, we normalize these functions such that $\sum_i \int F_i(\mathbf{k}')d^3\mathbf{k}'$ (the integrals are over the entire domain of definition of the integrands) is unity. This makes the definition of $W(P)$ unambiguous. Let us now study the implications of the abovementioned scaling relationship for the evolution of the shape of the density of states function

as well as for the relationship between the average frequency and the Debye frequency. If $h(\omega)$ is the density of states per degree of freedom (i. e. $\int h(\omega)d\omega = 1$) then

$$h(\omega) = 1/(24n\pi^3) \sum_i \int \delta(\omega - \omega_i(\mathbf{k}))d^3\mathbf{k} \quad (12)$$

The expression on the right hand side can be reduced, by using the scaling ansatz given in equation (11), to $(1/(24\pi^3W(P))H(\omega/W(P)))$ where $H(x) = \sum_i T_i(x)$ – with $T_i(x)$ being equal to $\int \delta(x - F_i(\mathbf{k}'))d^3\mathbf{k}'$. With these definitions average frequency $\langle \omega \rangle$ has the expression

$$\langle \omega \rangle = W(P) \left(\int xH(x)dx \right) / \left(\int H(x)dx \right) \quad (13)$$

It should already be obvious that the consequence of shape saturation is immediate. Similarly it can be shown that the Debye frequency ω_D satisfies the following relationship:

$$1/\omega_D^3 = (1/18\pi^2W^3(P)) \sum_j \overline{\left(\frac{1}{V_j^3(\hat{s})} \right)} \quad (14)$$

where the summation index j labels the three acoustic branches and $V_j(\hat{s}) = \lim_{x \rightarrow 0+} \frac{dF_j(x\hat{s})}{dx}$ (\hat{s} is a unit vector labelling a particular direction). The overhead bar denotes average over all directions.

To summarize, for a given potential, the scaling ansatz implies that both $\langle \omega \rangle$ and ω_D should be proportional to $W(P)$ with the two constants of proportionality being dependent on the state of aggregation. This would explain why the values of average frequency and Debye frequency computed for the three states of aggregation maintain the same mutual ratios at all (higher) pressures. It should be mentioned here that the power law scaling of average frequency (and hence Debye frequency, according to section III.C) with respect to pressure is not implied by the scaling ansatz. At the empirical level that is an additional feature.

We will now argue that for type A potentials the scaling ansatz should indeed be valid exactly as P goes to infinity. In the same limit we will show that the power law scaling of average or Debye frequency with respect to pressure should be exact. The steps involved in the argument are as follows: (i) With increasing pressure the interparticle distances keep on shrinking. For any generic potential that describes a stable solid the ratio of the repulsive part to the attractive part of the potential will keep increasing and eventually it will become permissible to ignore the attractive part altogether. For the potentials we are studying the repulsive part is always a sum-over-pairs of the various pair potentials. Thus, for type A potentials, the total potential energy has the following *effective* form at high pressures: $\sum_{i<j} (1/r_{ij}^m)$. In our particular calculation m is always a positive integer. (ii) Consider a stable equilibrium spatial arrangement of the particles in the solid for any of the three relevant states of aggregation at a pressure (let's say P_1) high enough for the effective form of the potential energy given above to be valid. Suppose we now consider

the situation at the somewhat higher pressure of $P_2 = \alpha P_1$. Because of the power law scaling of the potential energy (and hence forces) it should be clear that a configuration that has exactly the same geometry as the one at P_1 but has an overall contraction of the interparticle distances by a factor of $\alpha^{1/(3+m)}$ will be a stable equilibrium geometry at this new pressure P_2 . Now the elements of the dynamical matrix at wavevector \mathbf{k} are suitable Fourier transforms of the second derivatives of the potential energy with respect to various combinations of particle position coordinates. In this process of Fourier transformation the wavevector \mathbf{k} is multiplied by the Bravais lattice vectors which scale linearly with interparticle distances – which in turn is proportional to $n^{-1/3}$. Thus the \mathbf{k} dependence of the dynamical matrix will be only through the combination $\mathbf{k}n^{-1/3}$. We now relate the matrices of the second derivatives at P_1 and P_2 (before Fourier transformation). As noted above the spatial arrangements at P_2 and P_1 are different only by the scale of length. Since the pair potential has a power law form (proportional to r^{-m}) it is clear that the dynamical matrix (before Fourier transformation) at P_2 is that at P_1 multiplied $\alpha^{(2+m)/(3+m)}$. Finally, since the frequencies are square roots of the eigenvalues we get the desired result that $\omega(\mathbf{k})$ for a particular branch is indeed proportional to $P^{(2+m)/2(3+m)}$ multiplied by a function of the product $\mathbf{k}n^{-1/3}$. This is the scaling form that we have proposed earlier – with the additional specification that $W(P)$ itself has a power law form with the scaling exponent $\delta = (2+m)/(2(3+m))$ (which is obviously independent of the state of aggregation). So we see that the result III.A, which in principle is independent of the results in III.B and III.C, actually follows from the same line of reasoning that leads to the scaling ansatz that explains the results of III.B and III.C. In fact, after incorporating the power law dependence of density and the scale of vibrational frequency on pressure, the final scaling form of the dispersion relation is

$$\omega_i(\mathbf{k}) = ZP^{(2+m)/2(3+m)}G_i(P^{-1/(3+m)}\mathbf{k}) \quad (15)$$

(The arguments of G_i and F_i are different only through an overall constant of proportionality). This looks exactly like the standard scaling forms that are familiar in the theory of phase transitions and critical phenomena [47].

Given the centrality of the power law form of the pair potential in the preceding arguments how do we explain the empirical observation that even for type B potentials the properties of shape saturation of density of states and power law scaling of average/Debye frequencies are observed to a very good approximation over a very large ranges of pressure? To understand this we note that the key aspect of the argument given above is that at high pressures geometry of the arrangement of the particles should not change with pressure. For FCC and ideal HCP solids this is not an issue. For this to be possible for amorphous geometries the following condition has to be satisfied (we approximate the amorphous state by a periodic lattice with a large unit cell containing N particles) for $i = 1, 2, \dots, N$:

$$\nabla V_i(b\mathbf{r}_1, b\mathbf{r}_2, \dots, b\mathbf{r}_N) = q\nabla V_i(\mathbf{r}_1, \mathbf{r}_2, \dots, \mathbf{r}_N) \quad (16)$$

where b is a positive rescaling factor for interparticle distances. q , which is a function of b , is the rescaling factor for the forces. It is not difficult to see that this can be satisfied exactly only for type A potentials. Although type B potentials do not satisfy this exactly they can still satisfy, over a large but finite range of pressure, this to a very good degree of approximation. To see this we construct an effective power law exponent for pair potentials that are not actually of the power law form (Morse potential, for example). Since an arbitrary constant can always be added to a potential we construct the definition of the effective exponent in terms of the expression for the force $f(r)$ between a pair. For a power law potential $\ln(f(r))$ will be linear in $\ln(r)$ with a slope of $-(m+1)$. Hence a natural definition of the effective exponent at an interparticle separation of d is $-(dV''(d)/V'(d)+1)$ (Notice that this equals $\beta(d)-2$ where $\beta(d)$ is the function that controls the NDOSNF in the nearest neighbor approximation (section IV)). As expected, for a potential that is not of the power law type, this exponent is distance dependent. However, what really matters is how large is the value of the exponent and how much does it vary over the relevant range of pressures. For example, analysis of our data for the Morse potential shows that this exponent varies in the range of approximately 5 to 7 (and β varying from 7 to 9) in the regions of best linear fit in figure 3. It is this rather narrow range, caused by the rapid distance dependence of an exponentially decaying force, that is responsible for creating the impression of an almost saturating NDOSNF. To see why the exponent δ seems to be so well defined in figure 3, recall that δ is predicted to be $(2+m)/(2(3+m))$ for a power law potential with exponent m . This implies extremely weak dependence of δ on m . For example, when m varies from 5 to 10, δ varies only from 0.44 to 0.46. It is not thus surprising that the impression of an almost perfect linear fit is created in figure 3. The weak dependence of δ on m is due to the following reason: For larger values of m the nearest neighbor distance varies slowly with pressure but the spring constant that decides the scale of vibrational frequency varies rapidly with the nearest neighbor distance. For smaller values of m exactly the opposite happens. Thus, of the two factors that control the dependence of characteristic frequency on pressure, rapid variation in one is largely compensated by the slow variation of the other. It may be observed that the data in table I relating to the measured values of the exponent δ are indeed consistent, within the uncertainties of definition or measurement, with the prediction of $(2+m)/(2(3+m))$ where m is the true or effective power law exponent for the potential. We also understand from the formula for δ why it is always below 1/2.

The considerations presented above lead us to conclude that the saturation of the NDOSNF, mutual proportionality of the average and Debye frequencies and the power law dependence of the characteristic frequencies on pressure are rather robust results if one does not demand rigorous exactness. Hence these represent predictions that can be tested in experiments on real materials or

ab initio calculations provided the pressure is sufficiently high.

VI. Double isosbestic points in the spectra of type A amorphous systems

The nearest neighbor model of vibrational spectrum for FCC and ideal HCP, as discussed in section IV, has the property that the NDOSNF is decided for a given type of crystal structure entirely by the value of the parameter $\beta(d)$. However, this parameter actually does not depend on the nearest neighbor distance d for a type A potential in the limit of high pressure (for $\phi(r)$ proportional to r^{-m} the asymptotic value of β is $(2+m)$). This means that the NDOSNF asymptotically converges to a well defined limit for FCC and ideal HCP for type A potentials and this limit is decided by the value of m . At the end of section IV we noted that the NDOSNF has a well defined limit as β (or m) goes to infinity. Let us now consider the GLJ(m,n) family of potentials with a fixed value of $(m-n)$ but m assuming all positive integer values starting from, let's say, 12. If we consider the FCC or ideal HCP solids for any of these potentials the NDOSNF will saturate (the limit being determined by m) as pressure keeps increasing. Also this limiting curve itself will have a well defined limit when m tends to infinity.

What happens if we consider the *amorphous* state for these potentials [43]? The arguments of section IV are no longer applicable. Here the NDOSNF does display exact asymptotic saturation with respect to increasing pressure since we are dealing with type A potentials. However, unlike in the case of FCC and ideal HCP solids, this asymptotic NDOSNF does not have a well defined limit when m tends to infinity. Instead what happens is that the asymptotic NDOSNF displays two isosbestic points. To within the accuracy with which these two points can be located, their coordinates do not depend on the value of $(m-n)$ (figure 15) . Isosbestic points in vibrational spectra have been reported earlier also in the literature [9]. However, the interesting point about the present work is that the potentials involved are essentially of the simplest conceivable kind (simple power law soft potential). Hence, although an analytical understanding of this phenomenon of the existence of the isosbestic points is likely to be quite difficult there is atleast no needless theoretical complication.

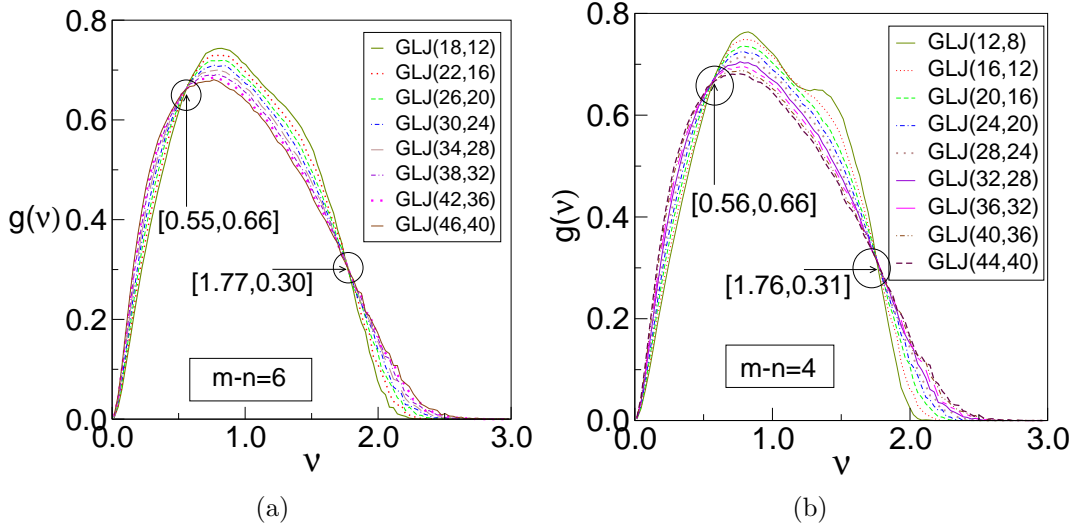


Figure 15: Existence of double isosbestic points in the superposition of normalized density of states $g(\nu)$ for normalized frequencies (ν) for the family of potentials $GLJ(m,n)$. The two isosbestic points are indicated by arrows. Their coordinates are also indicated. (a) For the family with $m - n = 6$. (b) For the family with $m - n = 4$. The coordinates of the two isosbestic points are the same in (a) and (b).

VII. Evolution of sound velocity with pressure

Study of sound propagation in materials under very high pressure is a subject of key importance in planetary geophysics [48-54]. Our present investigations afford us a way of studying this problem. Although our studies are at $T = 0$ this limitation is of much less serious consequence at the extreme high pressures that we are interested in. Inspired by the literature the two primary questions we have addressed in our studies are the following: (a) Does the ratio of transverse and longitudinal sound velocities saturate as pressure keeps growing? and (b) What are the limits of validity of the Birch's law [51] for linear relationship between density and sound speed?

Within the context of our studies based on model potentials answers to these questions can be found in the scaling form for the dispersion relationship that we have introduced. In fact it follows quite simply from the scaling law that both longitudinal and transverse speed of sound, after averaging uniformly over all angles, are proportional to $W(P)n^{-1/3}$ – immediately implying that ratio between the two averages approaches a constant at high pressures (where the scaling law is valid). For a power law potential with exponent m we have already found that: (1) the scaling law is exact, (2) P is proportional to $n^{m/3+1}$, and (3) $W(P)$ is proportional to P^δ with $\delta = (2 + m)/(2(3 + m))$. Thus, according to the scaling law, the two sound velocities should be proportional to $n^{m/6}$ or $P^{m/(2(3+m))}$ for a type A potential with exponent m . Validity of this can

be seen from figure 16 where a plot of $\ln(\text{velocity})$ versus $\ln(\text{number density})$ is shown for the three states of aggregation with GLJ(12,6) potential. In terms of the discussion above velocity should be proportional to the *square* of the density for this potential. This is indeed borne out by the data in fig.16. Also the ratio between the two computed average velocities approaches a constant as pressure keeps increasing. Thus we see that the Birch's law is certainly invalid for type A potentials at higher pressures except in the special case of $m = 6$.

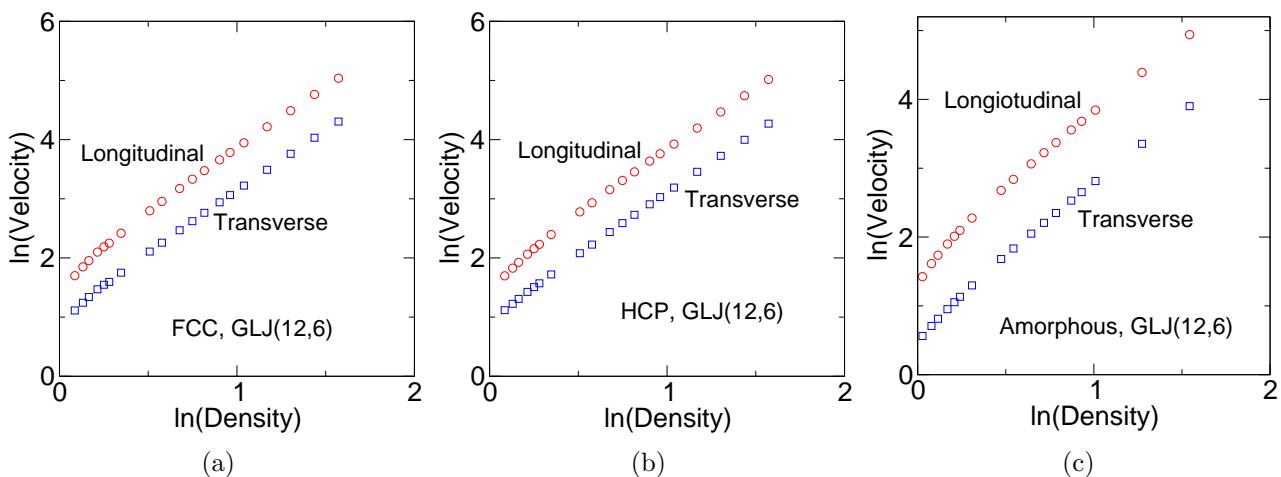


Figure 16: Log of sound velocity (longitudinal and transverse) versus log of density for the GLJ(12,6) potential. (a) FCC (b) HCP and (c) Amorphous. In all cases the slope at higher densities is 2 – showing that sound velocity is proportional to the square of density in that limit.

As a representative of type B potentials we examine the phenomenology of the Morse potential. We find that the ratio of the two direction averaged velocities never quite saturates. However, the deviation from saturation is very mild. For example, over a range of pressures (in the high pressure region) where density increases by a factor of 2 the ratio increases only by around 4 percent. Since this change is below the level of the typical error bar of an experimental measurement of this quantity it may justifiably be described as *de facto* saturation. At higher pressures average sound velocities show very close to linear variation with density for this potential – as can be seen from figure 17.

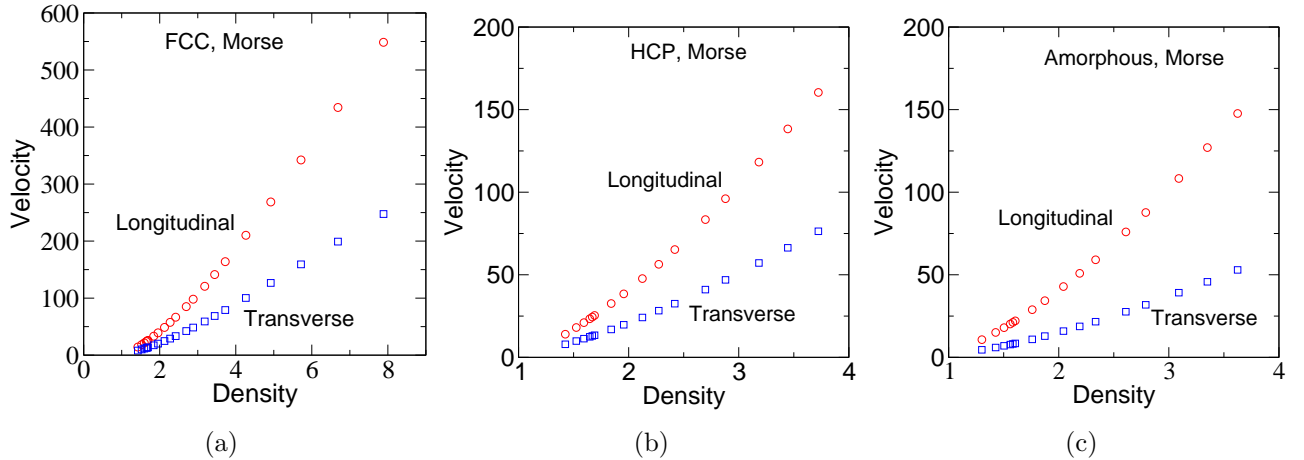


Figure 17: Plot of longitudinal and transverse sound velocities versus density for the Morse potential. (a) FCC (b) HCP and (c) Amorphous. In all cases the variation of sound velocity with density is linear to a very good approximation in a broad range of higher densities.

This behaviour is actually a consequence of the fact that in the pressure range under reference the effective exponent for the Morse potential varies in the range of 5 to 7. Combining this range for m with the prediction of $n^{m/6}$ variation of sound velocity, we can understand why an almost linear relationship (same as suggested by Birch's law) is found in this case over a rather large range of densities. However, even in this case data over a sufficiently large range of densities will indeed bring out the deviation from linear relationship quite clearly. The fact that the scaling law is not asymptotically exact in this case cannot be missed.

VIII. Comparison with data from experiments and *ab initio* calculations

None of the potentials used in the present work are considered to be candidates for describing any elemental solid over the wide pressure ranges in which we have performed our calculations. Moreover, the Morse and Gupta potentials are bounded above. So obviously they cannot describe the asymptotic pressure regions even in principle. Yet there are some qualitative and quantitative aspects of our calculations that can be tested against laboratory experiments or *ab initio* calculations. For example, we have argued at the end of section V that the mutual proportionality of average and Debye frequencies or their power law dependence on pressure are expected to be rather robust, even if not exact, results over rather wide range of high pressures. Figure 18 shows the data on the aspect of proportionality that we have found from reports of laboratory experiments. The three systems are bcc-iron ,hcp-iron and bct-tin with data taken from references 16, 17 and 19 , respectively. In all the cases the average frequency was calculated by us from the published density of states data.

The Debye frequency was taken directly from the references quoted for bct-tin and bcc-iron whereas it was calculated by us from the published vibrational density of states for hcp-iron.

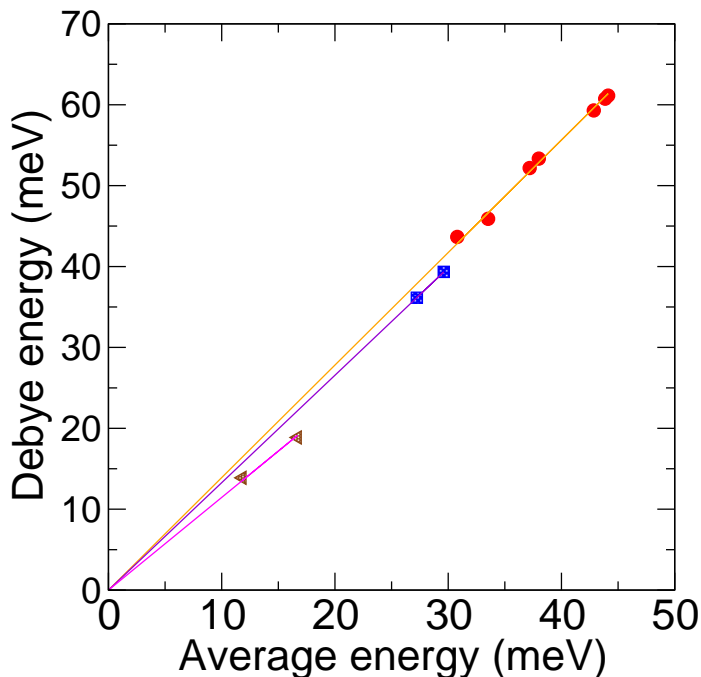


Figure 18: Average phonon energy is plotted against Debye energy for the data on crystalline spectra collected from literature. Circles: Experimental data for hcp-Fe [17]; Squares: Experimental data for bcc-Fe [16]; Triangles: Experimental data for bct-Sn [19]. Best fit straight line passing through origin is shown in each case.

Although none of the three cases cover the range of pressures that would be desirable for a satisfactory verification of the prediction of proportionality the data in all the cases are consistent with the expectation.

The verifiable quantitative predictions of our work follow from the following line of reasoning: In any real material the repulsive potential at the shorter distances is expected to grow faster than any power law i.e. the limit of pressure going to infinity should effectively be describable by a type A potential with the effective m becoming larger and larger at shorter distances – at least when the sum-over-pairs type of potential for the repulsive part is realistic. Several consequences follow from this. Below we point out these consequences and compare them with data available from laboratory experiments or *ab initio* calculations.

(i) When the applied pressure keeps increasing the NDOSNF for elemental solids should approach the β going to infinity limit of the NDOSNF in the nearest neighbor model. Earlier we mentioned that this limit of the nearest neighbor model is well defined. In fact the NDOSNF in this limit can be seen in figures 14(a) and 14(b) for FCC and ideal HCP, respectively. Figure 19 compares the

NDOSNF of HCP iron (the only HCP data we could find at such high pressures) from laboratory experiment as well as *ab initio* calculation at the highest available pressure (153 GPa) in [17] with the β going to infinity limit of the ideal HCP NDOSNF as shown in fig. 14(b). The agreement is quite satisfactory over the entire spectrum. We have not found analogous high pressure data for the FCC case that can be compared with the prediction shown in fig. 14(a).

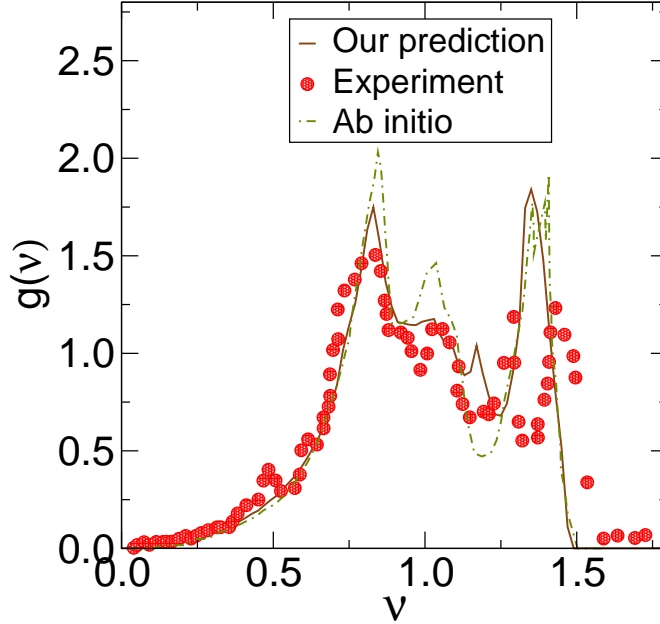


Figure 19: Normalized density of states $g(\nu)$ for normalized frequency (ν): comparison between our prediction and results from experiments/*ab initio* calculations for hcp-iron [17].

(ii) From the nearest neighbor model discussed in section IV we can calculate the ratio of the direction averaged longitudinal speed of sound ($\langle c_L \rangle$) and the corresponding value for transverse speed ($\langle c_T \rangle$). This ratio depends on the crystal type and the value of β . As we have discussed above the extreme high pressure limit should correspond to β going to infinity. For the ideal HCP case $\langle c_L \rangle / \langle c_T \rangle$ is predicted by this procedure to be 1.77 (in comparison, this ratio is 3.65 when β approaches 8 from above) and this is *independent of the material*. We have found experimental/*ab initio* calculation based values for this ratio at high pressure for hcp-rhenium and hcp-iron from [17,18,48]. The highest pressure experimental values of the ratio are around 1.85 and 2.00 for rhenium and iron, respectively. The corresponding values found from *ab initio* calculations of the phonon density of states in the GGA approximation are 1.96 (rhenium) and 1.93 (iron). These values, from experiments and calculations, are to be compared with the prediction of 1.77 from our approach.

(iii) The considerations for the HCP structure given in the immediately preceding paragraph can be extended to the FCC type also. Here the reported high pressure experimental data are

available in the form of the three independent elastic constants C_{11} , C_{12} and C_{44} . We have found data only for the inert element solids helium, neon, xenon, argon and krypton [20-23]. From these three independent elastic constants we can calculate two independent ratios involving the direction dependent speeds of transverse acoustic (TA) and longitudinal acoustic (LA) waves [21]: $(c_{LA,max}/c_{TA,max})^2 = (C_{11} + 2C_{12} + 4C_{44})/3C_{44}$ and $(c_{LA,max}/c_{LA,min})^2 = (C_{11} + 2C_{12} + 4C_{44})/3C_{11}$.

In table II we show how the experimental values for these two ratios from the laboratory experiments compare with our predictions. Please note that *all* FCC elemental solids are predicted to have the same values for these two ratios. While the agreement between the predicted and measured values of $(c_{LA,max}/c_{LA,min})^2$ is remarkably close in all cases, the situation is somewhat mixed for the other ratio. It is interesting to speculate on the possible role of many-body forces in causing these deviations. Presence of such forces, which is reflected in the deviation from Cauchy relationship between C_{12} and C_{44} , has been demonstrated in the case of argon [21]. In our models the potential is always effectively of the sum-over-pairs type at the highest pressures.

Table II: Comparison for ratios of sound velocities in FCC systems: experiment versus our prediction

System	Highest Pressure (GPa)	$\frac{C_{11}+2C_{12}+4C_{44}}{3C_{44}}$		$\frac{C_{11}+2C_{12}+4C_{44}}{3C_{11}}$	
		Experimental value	Prediction of present work	Experimental value	Prediction of present work
He (Ref. 20)	0.493	2.65	2.67	1.34	1.34
Ne (Ref. 23)	7	3.65		1.36	
Ar (Ref. 21)	70	3.04		1.30	
Kr (Ref. 23)	8	3.47		1.31	
Xe (Ref. 23)	10.6	3.19		1.34	

IX. Concluding remarks

In this paper we have demonstrated that certain aspects of the vibrational spectra and related properties in isotropically interacting solids at high pressures can be captured quite well by extrapolating the behaviour of simple model solids. Towards this end we have studied numerically various model solids in three different states of aggregation. For the crystalline states we have also studied a nearest neighbor interaction model. Although we have an analytical expression for the dynamical matrix for this model calculation of the density of states has been done only on computers. It would be desirable to solve this problem analytically for a finite value of the sole parameter (β) of the model for the various crystal structures involved. A somewhat simpler problem to solve would be the version where β is set to infinity right at the beginning.

We have also formulated a scaling law for the dispersion relations alongwith a justification for its applicability to certain types of potentials. An aspect of this work that perhaps needs improvement is the formulation of this scaling law for the amorphous case. Here the presence of a unit cell is artificial and the use of a Bloch vector is problematic. The challenge is to formulate the scaling properties in a manner that does not depend in an essential way on these artificialities.

For crystalline cases we should note that the asymptotic predictions made for various properties here are characteristic only of the crystal type and hence are applicable to *all* elemental solids belonging to that crystal type provided the interaction is isotropic and the repulsive part can be adequately described in terms of sum-over-pairs type potential in the high pressure limit. Thus there are significant elements of universality in the predictions. Data available from experiments are presently rather limited. In particular we have not found any data on the density of states at high enough pressures for an FCC system. But whatever data we have access to show reasonable to very good agreement with our predictions. Similar experiments and *ab initio* calculations on other elemental solids would provide further testing ground for the validity and utility of this work. Finally, we would like to draw attention to the extraordinary agreement between experimental data for five different FCC type inert element solids and our prediction for the ratio $(c_{LA,max}/c_{LA,min})^2$. Does it imply something more fundamental than we are able to see? This question becomes even more relevant when we notice that the agreement between experimental data for these same systems and our prediction is not nearly as close for the ratio $(c_{LA,max}/c_{TA,max})^2$.

Acknowledgements

D.S. thanks CSIR, India for financial support. Computational facility for this work has been funded by the FIST and UPOE programs of the Government of India.

References

1. R. J. Bell, Reports on Progress in Physics **35**, 1315 (1972).
2. T. S. Grigera, V. Martín-Mayor, G. Parisi, and P. Verrocchio, Phys. Rev. Lett. **87**, 085502 (2001); Nature (London) **422**, 289 (2003).
3. T. S. Grigera, A. Cavagna, I. Giardina, and G. Parisi, Phys. Rev. Lett. **88**, 055502 (2002).
4. W. Schirmacher, G. Diezemann, and C. Ganter, Physica B **284-288**, 1147 (2000); Phys. Rev. Lett. **81**, 136 (1998).
5. F. H. Stillinger and T. A. Weber, Phys. Rev. A **25**, 978 (1982).
6. A. Rahman, M. J. Mandell, and J. P. McTague, J. Chem. Phys. **64**, 1564 (1976).
7. M. Parrinello and A. Rahman, Phys. Rev. Lett. **45**, 1196 (1980).
8. M. Sampoli, P. Benassi, R. Eramo, L. Angelani, and G. Ruocco, J. Phys. : Cond. Matt. **15**, S1227 (2003);
9. C. A. Angell *et al*, J. Phys.: Cond. Matt. **15**, S1051 (2003).
10. H. R. Schober, J. Phys.: Condens. Matter **16**, S2659-S2670(2004).
11. L. V. Heimendahl and M. F. Thorpe, J. Phys. F: Metal Physics **5**, L87 (1975).
12. J. J. Rehr and R. Alben, Phys. Rev. B **16**, 2400 (1977).
13. *Amorphous Solids: Low Temperature Properties*, edited by W. A. Philips (Springer-Verlag, Berlin, 1981).
14. S. N. Taraskin and S. R. Elliott, *Vibrations in Disordered Systems* (Oxford University Press Inc., USA, 2004).
15. R. Lübbbers, H. F. Grünsteudel, A. I. Chumakov, and G. Wortmann, Science **287**, 1250 (2000); G. Shen *et al*, Phys. Chem. Minerals **34**, 353 (2004).
16. S. Klotz and M. Braden, Phys. Rev. Lett. **85**, 3209 (2000).
17. H. K. Mao *et al*, Science **292**, 914 (2001).
18. G. Steinle-Neumann, L. Stixrude, and R. E. Cohen, Phys. Rev. B **60**, 791 (1999).
19. H. Giefers *et al*, Phys. Rev. Lett. **98**, 245502 (2007).

20. J. Eckert, W. Thomlinson, and G. Shirane, *Phys. Rev. B* **16**, 1057 (1977).
21. H. Shimizu, H. Tashiro, T. Kume, and S. Sasaki, *Phys. Rev. Lett.* **86**, 4568 (2001).
22. H. Shimizu, N. Saitoh, and S. Sasaki, *Phys. Rev. B* **57**, 230 (1998).
23. S. Sasaki, N. Wada, T. Kume, and H. Shimizu, *J. Raman Spectroscopy* **40**, 121 (2009).
24. J. K. Dewhurst, R. Ahuja, S. Li, and B. Johansson, *Phys. Rev. Lett.* **88**, 075504 (2002).
25. H. Kobayashi *et al*, *Phys. Rev. Lett.* **93**, 195503 (2004).
26. V. V. Struzhkin *et al*, *Phys. Rev. Lett.* **87**, 255501 (2001).
27. S. Ghose *et al*, *Phys. Rev. Lett.* **96**, 035507 (2006).
28. A. P. Cantor *et al*, *Phys. of the Earth and Planetary Interiors* **164**, 83 (2007).
29. M. Yamaguchi, T. Nakayama, and T. Yagi, *Physica (Amsterdam)* **263B** 258 (1999); S. Sugai and A. Onodera, *Phys. Rev. Lett.* **77**, 4210 (1996).
30. B. Frick and C. Alba-Simionesco, *Physica (Amsterdam)* **266B**, 13 (1999); *Appl. Phys. A* **74** [Suppl.], S549-S551 (2002).
31. Y. Inamura, M. Arai, T. Otomo, N. Kitamura, and U. Buchenau, *Physica B* **284-288**, 1157 (2000); Y. Inamura, M. Arai, M. Nakamura, T. Otomo, N. Kitamura, S. M. Bennington, A. C. Hannon, and U. Buchenau, *J. of Non-Crystalline Solids* **293-295**, 389 (2001).
32. P. Jund and R. Jullien, *J. Chem. Phys.* **113**, 2768 (2000); O. Pilla, L. Angelani, A. Fontana, J. R. Goncalves, and G. Ruocco, *J. Phys.: Condens. Matter* **15**, S995 (2003).
33. R. J. Hemley, C. Meade, and H. K. Mao, *Phys. Rev. Lett.* **79**, 1420 (1997).
34. J. Schroeder, W. Wu, J.L. Apkarian, M. Lee, L. -G. Hwa, and C. T. Moynihan, *J. Non-Cryst. Solids* **349**, 88 (2004).
35. K. S. Andrikopoulos, D. Christofilos, G. A. Kourouklis, and S. N. Yannopoulos, *J. of Non-Crystalline Solids* **352**, 4594 (2006).
36. B. Begen, A. Kisliuk, V. N. Novikov, A. P. Sokolov, K. Niss, A. Chauty-Cailliaux, C. Alba-Simionesco, and B. Frick, *J. Non-Cryst. Solids* **352**, 4583 (2006).
37. K. Niss, B. Begen, B. Frick, J. Ollivier, A. Beraud, A. Sokolov, V. N. Novikov, and C. Alba-Simionesco, *Phys. Rev. Lett.* **99**, 055502 (2007).

38. A. Monaco, A. I. Chumakov, Y. -Z. Yue, G. Monaco, L. Comez, D. Fioretto, W. A. Crichton, and R. Rüffer, Phys. Rev. Lett. **96**, 205502 (2006); A. Monaco, A. I. Chumakov, G. Monaco, W. A. Crichton, A. Meyer, L. Comez, D. Fioretto, J. Korecki, and R. Rüffer, Phys. Rev. Lett. **97**, 135501 (2006).
39. A. I. Chumakov, I. Sergueev, U. van Bürck, W. Schirmacher, T. Asthalter, R. Rüffer, O. Leupold, and W. Petry, Phys. Rev. Lett. **92**, 245508 (2004).
40. N. Xu, M. Wyart, A. J. Liu, and S. R. Nagel, Phys. Rev. Lett. **98**, 175502 (2007); M. Wyart, L. E. Silbert, S. R. Nagel, and T. A. Witten, Phys. Rev. E **72**, 051306 (2005).
41. S. K. Sarkar, G. S. Matharoo and A. Pandey, Phys. Rev. Lett. **92**, 215503 (2004).
42. G. S. Matharoo, S. K. Sarkar, and A. Pandey, Phys. Rev. B **72**, 075401 (2005).
43. G. S. Matharoo and S. K. Sarkar, Phys. Rev. B **74**, 144203 (2006).
44. P. B. Allen, W. Garber, and L. Angelani, arXiv:cond-mat/0307435v2.
45. M. Born and K. Huang, *Dynamical Theory of Crystal Lattices* (Oxford University Press,1954).
46. N. W. Ashcroft and N. D. Mermin, *Solid State Physics* (Saunders College, Philadelphia, 1976).
47. Shang-Keng Ma, *Modern Theory of Critical Phenomena* (Benjamin/Cummings, Reading, 1976).
48. H. K. Mao *et al*, Nature **396**, 741 (1998); Nature **399**, 280 (1999).
49. G. Fiquet, J. Badro, F. Guyot, and H. Requardt, Science **291**, 468 (2001).
50. L. S. Dubrovinsky, N. A. Dubrovinskaia, and T. Le Bihan, Proc. Natl. Acad. Sciences **98**, 9484 (2001).
51. F. Birch, Geophys. J. R. Astron. Soc. **4**, 295 (1961); J. Geophysical Research **66**, 2199 (1961).
52. A. J. Campbell and D. L. Heinz, Science **257**, 66 (1992).
53. Jung-Fu Lin *et al*, Science **308**, 1892 (2005).
54. D. H. Chung, Science **177**, 261 (1972).